American Mineralogist, Volume 96, pages 1878–1893, 2011

Replacement of pyrrhotite by pyrite and marcasite under hydrothermal conditions up to 220 °C: An experimental study of reaction textures and mechanisms

Gujie Qian,[1,2] Fang Xia,[2,3] Joël Brugger,[2,3] William M. Skinner,[1] Jiafang Bei,[4] Guorong Chen,[5] and Allan Pring[2,3,*]

[1]Ian Wark Research Institute, University of South Australia, Mawson Lakes, South Australia 5095, Australia
[2]Department of Mineralogy, South Australian Museum, North Terrace, Adelaide, South Australia 5000, Australia
[3]Centre for Tectonics, Resources and Exploration (TRaX), School of Earth and Environmental Sciences, University of Adelaide, Adelaide, South Australia 5005, Australia
[4]School of Chemistry and Physics, University of Adelaide, Adelaide, South Australia 5005, Australia
[5]Key Laboratory for Ultrafine Materials of Ministry of Education, School of Materials Science and Engineering, East China University of Science and Technology, Shanghai 200237, China

Abstract

The transformation of pyrrhotite to Fe disulfide (pyrite and/or marcasite) under hydrothermal conditions was studied experimentally by probing the effects of temperature (up to 220 °C, vapor-saturated pressures), ΣS(-II) concentrations, pH, and availability of oxygen on reaction progress and on the resulting textures.

The pyrrhotite to Fe disulfide reaction proceeded by a dissolution-reprecipitation mechanism under all conditions. Marcasite and pyrite formed under both oxic and anaerobic conditions, which is inconsistent with the traditionally assumed polysulfide route for FeS_2 formation (oxidants required for polysulfide formation). The nature of the products was controlled by the level of supersaturation of the solution with respect to Fe disulfide minerals. Marcasite formed preferentially at low pH or S(-II)-deficient solutions (saturation index << 1000), while pyrite was the main product at saturation indices >1000.

Different textures were obtained for the replacement of pyrrhotite by either pyrite or marcasite. Pyrite formation proceeded by direct replacement of pyrrhotite and, simultaneously, by overgrowth from solution. The pyrite crystals were >10 μm in size and randomly oriented. In comparison, marcasite crystals were <1 μm in size, and no significant overgrowth was observed. At $pH_{21°C}$ <3, the marcasite nanocrystals showed the well-known crystallographic relationship with pyrrhotite, but at $pH_{21°C}$ 3.96, the marcasite crystallites were randomly oriented. These experimental results confirm that the preservation of the crystallographic orientation is not a distinguishing feature between dissolution-reprecipitation and solid-state reactions. The different textures among pyrite and marcasite reflect the dominance of crystal growth (pyrite) vs. nucleation (marcasite) as a precipitation mechanism.

Keywords: Hydrothermal replacement, pyrrhotite alteration, pyrite, and marcasite, dissolution-reprecipitation reaction, crystallographic relationship, textures

Introduction

The most widespread Fe sulfide minerals, pyrrhotite ($Fe_{1-x}S$, x = 0~0.125), pyrite (cubic FeS_2), and marcasite (orthorhombic FeS_2), are commonly associated with mineralization of various types, and are important S-bearing phases in many rocks, including coal, sedimentary, and metamorphic rocks (Murowchick 1992). Pyrrhotite is a nonstoichiometric compound with the NiAs-type structure (Thomas et al. 2001; Wang and Salveson 2005). Although many"polytypes" or ordered supercell forms are known, there are two basic subgroups: the hexagonal pyrrhotites with compositions centering on $Fe_{10}S_{11}$, and the Fe-depleted monoclinic pyrrhotites with compositions generally around Fe_7S_8 (Vaughan and Craig 1978). In many ore deposits, pyrrhotite has partially or completely been replaced by pyrite or marcasite (e.g., Einaudi 1971; Fleet 1978; Ramdohr 1980). Pyrite commonly contains pyrrhotite inclusions, indicating that early pyrrhotite has been replaced by pyrite, especially along evolving temperature and redox gradients (e.g., Mernagh et al. 2004; Sung et al. 2009).

The transformation of pyrrhotite to pyrite, sometimes with marcasite as an intermediary, results in various textures (Fig. 1), and correct interpretation of textures is important for deciphering the evolution of mineralizing systems (Murowchick 1992). Secondary marcasite replacing pyrrhotite is found either to display three preferred orientations, reflecting the hexagonal symmetry of the NiAs-type subcell of the parent pyrrhotite (Fleet 1978; pathway 1 in Fig. 1), or with random orientations (Murowchick 1992; pathway 2 in Fig. 1). In contrast, pyrite that directly replaces pyrrhotite usually lacks an orientational relationship with the parent grains (Murowchick 1992; pathway 2 in Fig. 1). Micrometer-size gaps, often filled with various accessory minerals such as hisingerite, siderite, and magnetite, are often

* E-mail: Allan.Pring@samuseum.sa.gov.au

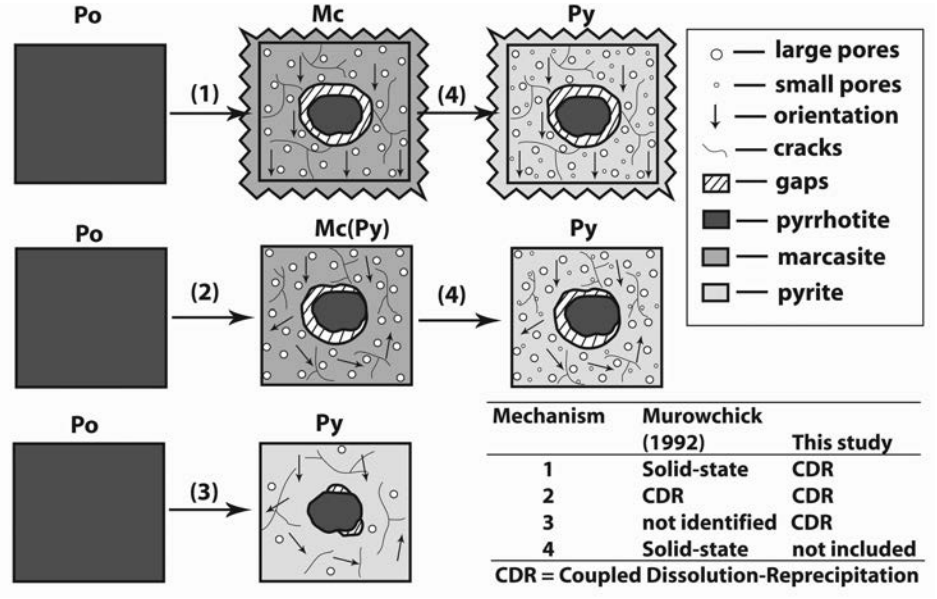

FIGURE 1. Schematic diagrams of pyrrhotite to FeS_2 replacement textures created according to literature. (1) Pyrrhotite to marcasite replacement, producing marcasite (and its overgrowth) with preferred orientations and large porosity (Fleet 1978). (2) Pyrrhotite replaced by marcasite (or pyrite), giving marcasite (or pyrite) with random orientations and large porosity (Murowchick 1992). (3) Pyrrhotite replaced by pyrite, with less porosity than the former cases and unspecified orientations (e.g., Fig. 545 in Augustithis 1995). (4) Marcasite to pyrite transformation via solid-state reaction, producing pyrite with preferred or random orientations and additional numerous small pores that corresponds to a volume change of –2.6% (Fleet 1978; Murowchick 1992). The formation of randomly oriented pyrite crystallites from marcasite in step 4 was indicated by Murowchick 1992. Note that the pore sizes, crack dimensions, and their numbers in these diagrams do not represent the real scales and proportions. Arrows with the same direction in steps 1 and 4 indicate minerals with preferred orientations; they do not represent a single orientation.

observed at the grain boundaries between the parent pyrrhotite and secondary Fe disulfide (Murowchick 1992; Ramdohr 1980). The newly formed pyrite and marcasite usually contain abundant micrometer-size pores, often filled with similar minerals; in some cases, however, the newly formed pyrite shows only minor porosity (pathway 3 in Fig. 1).

Murowchick (1992) suggested that the difference between replacement of pyrrhotite by crystallographically oriented marcasite (pathway 1 in Fig. 1) or by randomly oriented marcasite (pathway 2) was the result of different reaction mechanisms: a solid-state transformation results in a well-defined crystallographic orientation of the marcasite relative to the parent pyrrhotite, while a dissolution-reprecipitation mechanism leads to random crystallographic orientation of the neo-formed marcasite. Fleet (1978) first described the orientational relationships between pyrrhotite and neo-formed marcasite (based on the hexagonal pyrrhotite cell setting) as $\{10\bar{1}0\}_{po}||\{010\}_{mc}$, $\{0001\}_{po}||\{100\}_{mc}$, and $\{1\bar{2}10\}_{po}||\{001\}_{mc}$, and noted that the marcasite structure could be derived from that of pyrrhotite by the ordered removal of half of the Fe atoms from each (0001) vacancy-free plane. Collapse of the semi-vacated structure in the pyrrhotite **c**-axis direction accompanied by some contraction in the $[1\bar{1}00]$ direction could move the S atoms close enough to form disulfide pairs. Fleet (1978) did not explicitly propose a mechanism for the transformation of pyrrhotite to marcasite but suggested that the excess Fe generated would maintain the aqueous solution saturated with respect to marcasite, and that the excess Fe often reprecipitated as marcasite overgrowths on replacement marcasite (pathway 1 in Fig. 1). Fleet (1978) also noted that the secondary marcasite was porous and that this porosity was consistent with the 29% volume reduction associated with the transformation based on a constant S lattice (i.e., S immobile). Murowchick (1992) interpreted Fleet's (1978) work in terms of a solid-state diffusion driven process. In addition, Murowchick (1992) suggested that marcasite could precipitate directly from solutions after the dissolution of pyrrhotite at pH below 5 (e.g., Murowchick and Barnes 1986), and was thus an indicator of fluid chemistry during mineralization.

The replacement of pyrrhotite by pyrite has been postulated to occur either directly, or via a marcasite intermediary. Fleet (1978) postulated that pyrite observed in the studied natural assemblages was derived from inversion of earlier marcasite since the transformation of pyrrhotite to pyrite is not kinetically favored. Experimental studies have shown that marcasite readily transformed to pyrite via a solid-state process (a few hours at T > 450 °C under vacuum; Fleet 1970); this resulted in pyrite with two preferred orientation and a fine porosity (<1 μm) consistent with an overall volume reduction of 2.1%. These textures enabled recognition of pyrite that formed from a marcasite intermediary (pathway 1 → 4 in Fig. 1 of Murowchick 1992). However, many pyrites formed through conversion of pyrrhotite did not show preferred orientations relative to pyrrhotite, instead showing random orientations of crystallites (Fleet 1978). Murowchick (1992) proposed that some of these pyrites, showing a fine porosity, formed via the transformation of polycrystalline marcasite (pathway 2 → 4; Fig. 1), and that in other cases direct replace-

ment of pyrrhotite by pyrite (pathway 2 in Fig. 1) occurred by the oxidative dissolution of pyrrhotite followed by the direct precipitation of pyrite from solution at pH > 5.

In summary, Murowchick (1992) suggested that the preservation of crystallographic relationships between pyrrhotite and marcasite or pyrite implied a solid-state mechanism (pathways 1 → 4; Fig. 1), while the absence of crystallographic relation implied a dissolution-reprecipitation route. In recent years, several pseudomorphic mineral replacement reactions that also preserve crystallographic orientation have been shown to be interface coupled dissolution-reprecipitation replacement reactions rather than solid-state reactions as previously thought (see Putnis 2009 for a recent review). Instead of proceeding via solid-state diffusion, interface coupled dissolution-reprecipitation reactions involve the dissolution of the parent mineral in a fluid phase followed rapidly by precipitation of the daughter mineral forming a moving reaction interface coupled to the dissolution and precipitation steps. Interface coupled dissolution-reprecipitation replacement reactions can produce products that show either preferred orientation (e.g., Brugger et al. 2010; Putnis et al. 2005; Putnis 2007; Tenailleau et al. 2006; Xia et al. 2009a, 2009b) or random orientation (e.g., Qian et al. 2010; Zhao et al. 2009), depending on structural similarities between the parent and product minerals. The scale of the replacements can vary from the nanometer-scale to the micrometer-scale, depending on reaction conditions (e.g., Pewkliang et al. 2008; Qian et al. 2010; Xia et al. 2009a, 2009b).

Much work has been devoted to understanding the formation of pyrite and marcasite from aqueous solutions under diagenetic and hydrothermal conditions. Most studies emphasized the role of a fine-grained precursor phase, most commonly an "FeS" phase such as amorphous FeS, pyrrhotite, or mackinawite. Three main pathways have been proposed for pyrite and marcasite formation from "FeS" precursors. First, "FeS" can transform into FeS_2 via Fe-loss (e.g., Benning et al. 2000; Berner 1970; Butler et al. 2004; Wilkin and Barnes 1996), i.e., without the need for an external S(-II) source, as exemplified in the following reaction

$$2Fe_{1-x}S_{(po)} + (2-4x)H^+ = FeS_{2(mc)} + (1-2x)Fe^{2+}_{aq} + (1-2x)H_{2(g)} \quad \text{(Fe-loss pathway).} \quad (1a)$$

Second, pyrrhotite can be converted to pyrite following a sulfidation reaction mechanism in the presence of H_2S_{aq} (e.g., Drobner et al. 1990; Taylor et al. 1979a, 1979b)

$$Fe_{1-x}S_{(po)} + (1-2x)H_2S_{aq} = (1-x)FeS_{2(py)} + (1-2x)H_{2(g)} \quad (H_2S \text{ pathway}). \quad (2a)$$

Equations 1a and 2a occur under anaerobic conditions and produce $H_{2(g)}$ as a by-product (i.e., H^+ is the oxidant). Finally, Murowchick (1992) proposed that the reaction from pyrrhotite to Fe disulfide requires an external oxidant

$$2Fe_{1-x}S + (2-4x)H^+ + (½ - x)O_{2aq} = FeS_{2(s)} + (1-2x)Fe^{2+}_{aq} + (1-2x)H_2O \quad (O_2\text{-pathway}). \quad (3a)$$

In the present paper, we call this the "O_2-pathway", to emphasize the need for an external oxidant. Several studies have demonstrated that in the case of pathway 3a, aqueous polysulfides are important intermediaries (e.g., Murowchick 1992 and references therein); such polysulfides form for example by reaction of H_2S_{aq} with O_{2aq}

$$n\,H_2S_{aq} + ½(n-1)O_{2aq} = H_2S_{naq} + (n-1)H_2O (pH < 5). \quad (4)$$

The form of polysulfides depends on solution pH (H_2S_n at $pH_{25°C}$ <5; HS^-_n at $pH_{25°C}$ = 5~7; S^{2-}_n at $pH_{25°C}$ >7), and it is assumed that the presence of neutral polysulfides (i.e., H_2S_n) favor marcasite nucleation (Murowchick 1992; Murowchick and Barnes 1986; Schoonen and Barnes 1991).

Therefore, despite many years of studies on the transformation of pyrrhotite (and "FeS") to Fe disulfide, there are unresolved questions regarding the mechanisms of this reaction. Here we present the first systematic experimental study of the replacement of pyrrhotite by pyrite and marcasite. We studied the effect of various hydrothermal conditions (T up to 220 °C, pH, ΣS(-II) concentration, and oxygen availability) on reaction progress, nature of Fe disulfide, and resulting textures, with an attempt to identify the mechanisms responsible for the large diversity of textures observed for the replacement of pyrrhotite by Fe disulfide (Fig. 1).

Materials and methods

Pyrrhotite

Natural massive pyrrhotite (Nairne, South Australia; South Australian Museum Registration Number G7716) was used throughout this study. The pyrrhotite was first ultrasonically cleaned in deionized water to remove particulate surface contamination. Then, it was crushed and sieved into different grain size fractions, which were rewashed to remove fine adhering particles. The composition of the pyrrhotite determined by electron probe microanalysis (mean of 30 points) is $Fe_{0.89(2)}S$ (3σ given in parentheses) with traces of Mn (up to 0.1 wt%), Cu (to 0.1 wt%), Ni (to 0.08 wt%), and Co (to 0.08 wt%). Powder X-ray diffraction analysis showed no evidence for additional mineral phases, a result confirmed by the examination of sections using the scanning electron microscope. The pyrrhotite has weak magnetism and has no peak splitting in its powder X-ray diffraction pattern.

pH buffer solutions and pH measurements

The pH buffer solutions used in this study are summarized in Table 1. They were prepared at room temperature using Milli-Q water. The pH measurements were performed using a temperature-corrected pH/Ion/mV meter (EUTECH Scientific, model Cyberscan 510) with a Ag/AgCl pH probe. The precision of the probe is about 0.01. Calibrations were carried out using AQUASPEX standard buffer solutions: KH-phthalate buffer ($pH_{25°C}$ 4.01), phosphate buffer ($pH_{25°C}$ 7.00), and carbonate buffer ($pH_{25°C}$ 10.01). Note that pH will change with temperature

Table 1. Compositions of buffer solutions used in this work

	$pH_{21°C}$		Composition (in molal)
Buffer code	Calculated‡	Measured†	
A	0.97	0.96	0.1340 HCl + 0.0500 KCl
B	1.97	2.07	0.0130 HCl + 0.0500 KCl
C	3.02	2.93	0.0192 H_3PO_4 + 0.1808 NaH_2PO_4
D	2.54	2.45	0.0500 H_3PO_4 + 0.1500 NaH_2PO_4
E	4.00	3.96	0.1656 CH_3COOH + 0.0343 CH_3COONa
F	7.05	7.03	0.0347 NaH_2PO_4 + 0.0652 Na_2HPO_4
G	9.09	9.01	0.0500 H_3BO_3 + 0.0210 NaOH
H	10.70	10.78	0.1500 Na_2HPO_4 + 0.0240 NaOH
I	10.98	11.08	0.0250 Na_2HPO_4 + 0.0040 NaOH
J§	2.53	2.50	0.0030 HCl
K§	0.96	1.04	0.0543 H_2SO_4
L	2.65	2.57	3.5300 CH_3COOH + 0.0300 CH_3COONa

* The pH values were calculated by Geochemist's Workbench (Bethke 2008).
† Errors for the measured pH values are ±0.01.
‡ Not a buffer.

TABLE 2. Experimental conditions for pyrrhotite to Fe disulfide reactions under various conditions

Run	*T* (°C)	$pH_{21°C}$ start (buffer code)	pH_{calc} at high *T**	$pH_{21°C}$ end	TAA (mg)	Calc. ΣS(-II) (mmolal)	Time (h)	Filling gas	Po weight (mg)	Po size (μm)	wt% of products†
M1‖	125	2.45 (D)	3.05	2.58	50.0	36.0	336	Air	32.0	125–150	Po
M2‡	190	0.96 (A)	1.02	1.10	10.0	7.2	336	Air	32.0	125–150	Mc(93), Py(7)
M3	190	2.45 (D)	3.28	2.99	10.0	7.2	336	Air	32.0	125–150	Py(30), Po(24), $NaFe_3P_3O_{12}$(46)§
M4	190	3.96 (E)	4.53	4.10	10.0	7.2	336	Air	32.0	125–150	Py(28), Po(72)
M5‖	190	10.78 (H)	9.44	10.01	10.0	7.2	336	Air	32.0	125–150	Po
M6	190	0.96 (A)	1.02	1.20	50.0	36.0	336	Air	32.0	125–150	Mc(92), Py(8)
M7‖	190	2.45 (D)	3.28	2.83	50.0	36.0	336	Air	32.0	125–150	Py(58), Mc(11), Po(31)
M7-1‖	190	2.45 (D)	3.28	2.79	50.0	36.0	288	Air	20.0	125–150	Py(33), Mc(9), Po(58)
M8	190	3.96 (E)	4.53	4.09	50.0	36.0	336	Air	32.0	125–150	Po
M9‖	190	10.78 (H)	9.44	8.23	50.0	36.0	336	Air	32.0	125–150	Po
M10	190	0.96 (A)	1.02	1.30	100.0	72.0	336	Air	32.0	125–150	Mc(82), Py(18)
M11‖	190	2.45 (D)	3.28	3.63	100.0	72.0	336	Air	32.0	125–150	Po
M12	190	3.96 (E)	4.53	4.04	100.0	72.0	336	Air	32.0	125–150	Po
M13‖	190	10.78 (H)	9.44	7.28	100.0	72.0	336	Air	32.0	125–150	Po
M14	220	0.96 (A)	1.05	1.18	50.0	36.0	336	Air	32.0	125–150	Mc(95), Py(5)
M15‖	220	2.45 (D)	3.36	2.91	50.0	36.0	336	Air	32.0	125–150	Py(55), Mc(19), Po(26)
M16	220	3.96 (E)	4.70	4.08	50.0	36.0	336	Air	32.0	125–150	Py(15), Po(85)
M17‖	220	10.78 (H)	9.38	8.34	50.0	36.0	336	Air	32.0	125–150	Po
M18#	190	0.96 (A)	1.02	1.32	50.0	36.0	24	Air	53.0	125–150	Mc(91), Py(9)
M19**	190	0.96 (A)	1.02	1.36	50.0	36.0	24	N2	53.0	125–150	Mc(92), Py(8)
M20	190	0.96 (A)	1.02	1.04	–	–	2	Air	32.0	125–150	Mc(37), Po(63)
M21	190	0.96 (A)	1.02	1.06	–	–	2	N2	32.0	125–150	Mc(35), Po(65)
M22	125	0.96 (A)	0.96	1.01	–	–	2	Air	32.0	125–150	Mc(15), Po(85)
M23	125	0.96 (A)	0.96	1.08	–	–	168	N2	32.0	400–1000	Mc(94), Py(6)
M24	125	3.96 (E)	4.23	4.34	–	–	168	N2	32.0	400–1000	Mc(9), Po(91)
M25	190	3.96 (E)	4.53	4.17	40.0	28.8	984	N2	32.0	125–150	Po
M26	190	3.96 (E)	4.53	4.26	40.0	28.8	984	Air	32.0	125–150	Py(29), Po(71)
M27‖	190	10.78 (H)	9.44	8.17	50.0	36.0	840	Air	32.0	53–90	Py(9), Po(91)
M28	125	3.96 (E)	4.23	4.03	–	–	168	N2	42.0	400–1000	Mc(8), Po(92)
M29	125	0.96 (A)	0.99	1.22	30.0	21.6	168	Air	42.0	400–1000	Mc(94), Py(6)
M30	125	2.07 (B)	1.98	2.89	30.0	21.6	168	Air	42.0	400–1000	Py(15), Po(85)
M31‖	125	2.93 (C)	3.52	3.43	30.0	21.6	168	Air	42.0	400–1000	Po
M32	125	3.96 (E)	4.07	4.23	30.0	21.6	168	Air	42.0	400–1000	Po
S1	125	0.96 (A)	0.99	1.19	–	–	168	Air	42.0	400–1000	Mc(91), Py(9)
S2	125	2.07 (B)	1.98	2.76	–	–	168	Air	42.0	400–1000	Mc(33), Py(5), Po(62)
S3	125	2.93 (C)	3.52	3.17	–	–	168	Air	42.0	400–1000	Mc(32), Po(68)
S4	125	3.96 (E)	4.07	4.05	–	–	168	Air	42.0	400–1000	Mc(28), Po(72)
S5	125	7.03 (F)	7.16	6.86	–	–	168	Air	42.0	400–1000	Po
S6	125	9.01 (G)	8.52	8.34	–	–	168	Air	42.0	400–1000	Po
S7	125	11.08 (I)	9.36	7.11	–	–	168	Air	42.0	400–1000	Po
S8	125	10.78 (H)	9.84	8.23	–	–	672	Air	42.0	20–38	Hm(13), Mc(8), Py(4), Po(75)

* pH values at high temperatures were calculated using Geochemist's Workbench.
† Weight fractions were given in brackets; errors of wt% of products are around ±3% (3σ); Py = Pyrite, Mc = Marcasite, Po = Pyrrhotite, Hm = Hematite.
‡ 12.2 mg reaction products.
§ PDF number: 45-0126.
‖ EDS analysis found no Fe phosphate on the pyrrhotite surface (when phosphate buffers were used for pH control).
20.6 mg reaction products were obtained. Solution ICPMS analysis of the post reaction solution gave 1183(22) ppm Fe.
** 18.9 mg reaction products were obtained.

because equilibrium constants and ionic strengths are temperature dependent (e.g., Tables 1 and 2). To avoid confusion, the measured pH values at room temperature are used throughout the text.

The effect of buffer species on our results was also investigated by duplicating experiments at two similar pH values using different buffers (Table 3). The use of different buffers did not affect the textures or the nature of the reaction products, confirmed by optical microscopic studies and powder XRD analysis. The nature of the buffer species had a minor effect on the kinetics of the reaction.

Hydrothermal experiments

All hydrothermal replacement reactions were carried out in polytetrafluoroethylene (PTFE)-lined stainless steel autoclaves (volume: ~23.5 mL) placed in furnaces at temperatures between 125 and 220 °C (±1 °C) and under vapor-saturated pressures. Accurately weighed pyrrhotite grains and 18.5 mL of buffer solution were loaded into the autoclaves, leaving ~5 mL of air gap to allow fluid thermal expansion at reaction temperatures. Hydrothermal experiments under near-anaerobic conditions were prepared as follows. Fresh acetate buffer solutions were made with deoxygenated deionized water with the aid of a vacuum line continuously flushed with N_2 (99.999%; BOC). The solutions were immediately transferred to a N_2-filled glove box, where the buffer solutions, pyrrhotite grains and TAA were loaded into the autoclaves, leaving ~5 mL of N_2 gap.

TABLE 3. Reaction extent vs. time at different pH and at 190 °C*

$pH_{21°C}$ 0.96/$pH_{190°C}$ 1.02 (A)			$pH_{21°C}$ 1.04/$pH_{190°C}$ 1.59 (K)		
Run code	Time (h)	Mc, Py (wt%)	Run code	Time (h)	Mc, Py (wt%)
N1	1	40, 4	N4	1	26, 5
N2	2	66, 4	N5	2	54, 5
N3	3.5	90, 7	N6	3.5	77, 8
$pH_{21°C}$ 2.45/$pH_{190°C}$ 3.28 (D)			$pH_{21°C}$ 2.57/$pH_{190°C}$ 3.26 (L)		
Run code	Time (h)	Mc, Py (wt%)	Run code	Time (h)	Mc, Py (wt%)
N7	92	0, 16	N11	92	0, 9
N8	164	5, 32	N12	164	3, 24
N9	216	13, 42	N13	216	9, 34
N10	257	15, 52			
$pH_{21°C}$ 3.96/$pH_{190°C}$ 4.53 (E)			$pH_{21°C}$ 10.78/$pH_{190°C}$ 9.44 (H)		
Run code	Time (h)	Py (wt%)	Run code	Time (h)	Po (wt%)
N14	744	9	N17	744	100
N15	1056	18	N18	1056	100
N16†	1320	27	N19	1320	100

* Py = pyrite, Mc = Marcasite, Po = pyrrhotite; errors of the wt% of the products are around ±3%. Each experimental run was conducted, using 32.0 mg pyrrhotite of 125–150 μm grain size, in the presence of 60.0 mg thioacetamide [equivalent to 43.2 mmolal ΣS(-II)]. Buffer code was also given in the table.
† Mass of reaction products: 32.3 mg; Fe concentration in quenched solution was around 42(1) ppm from solution ICPMS analysis.

External S(-II) source was introduced in the form of thioacetamide (≥99%; hereafter denoted as TAA; Table 2). TAA breaks down upon heating to produce H_2S [or other forms of S(-II), depending on pH]

$$CH_3CSNH_2 + H_2O \rightarrow CH_3CONH_2 + H_2S_{aq}. \quad (5)$$

TAA was selected as an S(-II) source rather than e.g., NaHS, Na_2S, because these sodium sulfides are basic, and their use could seriously affect the pH of acidic buffer solutions. The fast dissociation of TAA was verified by adding 60 mg TAA together with 18.5 mL $pH_{21°C}$ 3.96 acetate buffer solution into three autoclaves. The autoclaves were then placed in 140, 190, and 220 °C furnaces. After 5 h, the autoclaves were quenched in water and the solutions were immediately mixed with 20 mL 0.05 *M* $Pb(CH_3COO)_2$ solutions. Solutions with black precipitate (PbS) were filtrated and washed by water and acetone three times in three sintered glass filter crucibles. The PbS precipitates were then oxidized by H_2O_2 into $PbSO_4$. After further washing, the $PbSO_4$ precipitates were dried in an 80 °C oven until constant weights. The weight of $PbSO_4$ obtained from the 220, 190, and 140 °C runs were 191.5 mg (corresponding to 79% decomposition of TAA), 182.3 mg (75%), and 176.7 mg (73%), respectively. For reasons of clarity, the corresponding concentration of ΣS(-II) (mainly in the form of H_2S, HS^- with very minor S^{2-}; Rickard and Luther 2007) calculated by assuming total hydrolysis of TAA (Eq. 5) is used throughout the following text. Most reactions were performed over a much longer time scale, so this is a reasonable assumption.

Instrumentation and analytical methods

Room-temperature powder X-ray diffraction (XRD) patterns of post-quenched products were obtained on a Huber Guinier Imaging Plate Camera G670 with Co$K\alpha_1$ X-radiation (λ = 1.78892 Å). The samples were ground in acetone, spread uniformly on a mylar (polyethylene terephthalate) film, and then mounted onto the sample oscillation unit for data collection. Normally a 15 min exposure resulted in a high-quality diffraction pattern suitable for quantitative phase analysis. The absence of sample oxidation during sample preparation and XRD analysis was tested by comparing the analysis of sample M7 prepared using the standard procedure with that of an aliquot prepared under anoxic conditions. This second aliquot was prepared in a glove box filled with 99.999% BOC N_2. The sample was crushed and ground for ~1 min and then sealed between two layers of KAPTON film [polyimide; strong O_2(g) impermeability; see Table 5 in Schmitz and Janocha 2000]. Rietveld refinement of the resulted XRD pattern showed that the sample prepared in N_2 contained 57 ± 3 wt% pyrite, 11 ± 3 wt% marcasite, and 32 ± 3 wt% pyrrhotite, and showed negligible differences with the phase percentages of the sample prepared in air (analysis reported in Table 2).

Quantitative phase analysis was performed by the Rietveld method (Rietveld 1967, 1969) using Rietica for Windows version 1.7.7 (Hunter 1998). This method has been successfully applied to monitor the progress of mineral reactions (e.g., Putnis 2007; Qian et al. 2010; Wang et al. 2006; Xia et al. 2008, 2009a, 2009b; Zhao et al. 2009). In each refinement, the zero shift was taken from measurements of an external NBS640 Si standard. The background and phase scale were initially refined, followed by unit-cell parameters, and finally peak shape parameters. The background was fitted using a fifth-order polynomial function, and peak shape using a pseudo-Voigt (Howard Asymmetry) profile. Three standard deviations on the weight percent of products from the Rietveld refinement were used as a confidence level in the discussion of reaction progress. The initial crystal structure models of pyrite, marcasite, pyrrhotite, and hematite were taken from the ICSD database (pyrite code: 55699; marcasite code: 109374; pyrrhotite code: 1996; hematite code: 82902), and are originally sourced from Wu et al. (2004), Rieder et al. (2007), Koto et al. (1975), and Sawada (1996), respectively. We chose the monoclinic (pseudo-orthorhombic) pyrrhotite model (with no peak splitting) from Koto et al. (1975) for the following reasons: (1) monoclinic pyrrhotite models with peak splitting at high angles do not apply to the pyrrhotite used in this work; and (2) hexagonal pyrrhotite models do not reproduce the intensity of one diffraction peak of our pyrrhotite at the d spacing of 2.981(3) Å, but the model of Koto et al. (1975) provides an excellent agreement (e.g., Fig. 2). The calculated densities for pyrite, marcasite, and pyrrhotite from Rietveld refinements are 5.035, 4.853, and 4.712 g/cm^3, respectively. These densities were subsequently used to calculate the volume changes of pyrrhotite to Fe disulfide reactions.

Scanning electron microscope (SEM) images were obtained on a Philips XL30 field emission SEM equipped with an energy-dispersive X-ray spectrometer (EDS). Surface morphology and polished cross sections of reacted pyrrhotite grains were imaged under secondary and backscattered electron modes, respectively.

Electron backscatter diffraction (EBSD) analyses were performed using either an EDAX-TSL-EBSD system or a HKL EBSD system. The samples were first polished with diamond paste (3 and 1 µm) for 20 min, and then polished with a 0.04 µm colloidal silica suspension for 60 min to remove the damaged layer. After polishing, the samples were ultrasonically cleaned, dried, and coated with 1.5 nm thick carbon film to minimize electron charging. The EDAX-TSL EBSD system was fitted to a FEI Helios NanoLab DualBeam FIB/SEM platform. EBSD patterns were collected at 20 kV, 5.5 nA, and a step size of 0.25 µm using a Hikari camera at a working distance of 13.5 mm. Crystallographic data for pyrite and pyrrhotite were taken from the MINCRYST database (pyrite code: 3812; pyrrhotite code: 3889) and are originally sourced from Wyckoff (1963) and Tokonami et al. (1972), respectively. The software packages "Orientation Imaging Microscopy (OIM) DATA Collection v 5.2" and "OIM Analysis v 4.5" were used for data collection and interpretation, respectively. The HKL EBSD system was fitted to the Philips XL30 SEM. EBSD data were collected at 20 kV accelerating voltage and a working distance of 20 mm using a Nordlys camera. The HKL Channel 5 software package was used for data collection and interpretation. Crystal structural data for marcasite and pyrrhotite for HKL EBSD were from the ICSD database (marcasite code: 26756; pyrrhotite code: 29301) and are originally from Buerger (1931) and Alsen (1925), respectively.

Electron probe microanalysis (EPMA) (CAMECA SX51) was carried out to determine the composition of the natural pyrrhotite, using the following X-ray lines and external standards: Fe$K\alpha$/marcasite; S$K\alpha$ and Cu$K\alpha$/chalcopyrite; Mn$K\alpha$/rhodonite, Co$K\alpha$/metallic Co; Ni$K\alpha$/pentlandite. The analysis was undertaken using an accelerating voltage of 20 kV and a beam current of ~20 nA with wavelength-dispersive X-ray spectrometers (WDS) with counting times of 20 and 10 s for the elements and their backgrounds, respectively.

Solution ICP-MS (Agilent 7500ce) was utilized to analyze the Fe concentration in solutions after hydrothermal reactions. Solutions were collected from quenched autoclaves using Becton Dickinson Plastipak syringes and filtered by 0.45 µm Acrodisc syringe filters. ^{57}Fe and ^{56}Fe were both monitored for the Fe analysis. The differences between ^{57}Fe and ^{56}Fe results were within ±3%. Data from ^{57}Fe were used for calculation of Fe concentrations throughout this study.

Calculation of solubility indices and high-temperature pH were conducted using the Geochemist Workbench package (Bethke 2008). Thermodynamic properties were taken from the Lawrence Livermore National Laboratory database (ver. R9), except for Fe(II) chlorides (Testemale et al. 2009), HCl_{aq} (Pokrovskii 1999), and HS^-/H_2S_{aq} (Suleimenov and Seward 1997).

Results

The effect of pH

The effect of pH on the reaction products was studied at 190 °C with different ΣS(-II) concentrations (runs M2–M13, M27

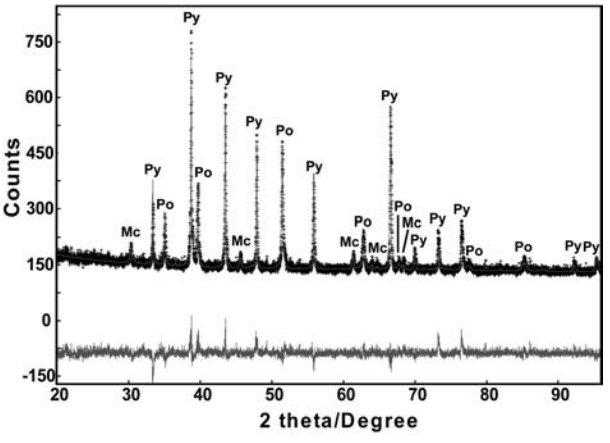

Figure 2. X-ray diffraction pattern and Rietveld refinement of partially transformed pyrrhotite (run M7; Table 2). The original data are in black; the gray line through the dark crosses is the calculated pattern; the gray line at the bottom is the difference between the original data and calculated (fitted) values. Goodness-of-fit parameters (R_p, R_{wp}, χ^2) for the Rietveld refinement are 3.865, 5.188, and 0.416, respectively. Po = Pyrrhotite, Py = Pyrite, Mc = Marcasite.

in Tables 2 and 3). The post-quenching XRD analysis showed that the pH affected the nature of Fe disulfide (e.g., Fig. 3a). With ≥7.2 mmolal ΣS(-II), marcasite was the predominant reaction product at $pH_{21°C}$ 0.96, while pyrite became the dominant product at $pH_{21°C}$ ≥2.45 (Fig. 3a; Table 3). In contrast, marcasite was always the dominant product under both acidic and basic pH conditions if no external S(-II) was added.

The effect of pH on the overall transformation rate (evaluated by reaction extents over reaction time) was studied at 190 °C in the $pH_{21°C}$ range of 0.96–10.78 with 43.2 mmolal ΣS(-II) (Table 3). In general, the overall reaction rate decreased with increasing pH (Fig. 3a); no reaction was observed at $pH_{21°C}$ 10.78 even after 1320 h. Note that experiments conducted at similar pH but with different "buffers" (A vs. K; D vs. L; Table 3) had similar reaction products and textures (similar reaction mechanism), but slightly different kinetics. This indicates that the ionic buffer species have a second-order influence on the kinetics of the reactions relative to pH.

The effect of ΣS(-II)

The availability of external S(-II) affected the nature of Fe disulfide at $pH_{21°C}$ >2 in this study. A series of experiments conducted at different pHs with or without addition of S(-II) (runs M29–M32 in Table 2 vs. runs S1–S4 in Fig. 4a and Table 2) revealed that in the absence of external S(-II), pyrrhotite generally transformed to marcasite with only minor amounts of pyrite under both acidic and basic conditions (Figs. 3b, 4a, and 4b). For example, the product from a $pH_{21°C}$ 2.07 experiment (run S2; Table 2 and Fig. 4a) with no S(-II) addition consisted of 33(3) wt% marcasite and 5(3) wt% pyrite. In the presence of external S(-II), marcasite formation was strongly inhibited. Run M30 [15(3) wt% pyrite and no detectable marcasite; Table 2] was performed under identical conditions to run S2 (Table 2 and Fig. 4a), except for the addition of 21.6 mmolal ΣS(-II). Direct comparison of experiments with and without external S(-II) at 190 °C and at $pH_{21°C}$ 2.45/2.50 and 3.96 also confirmed

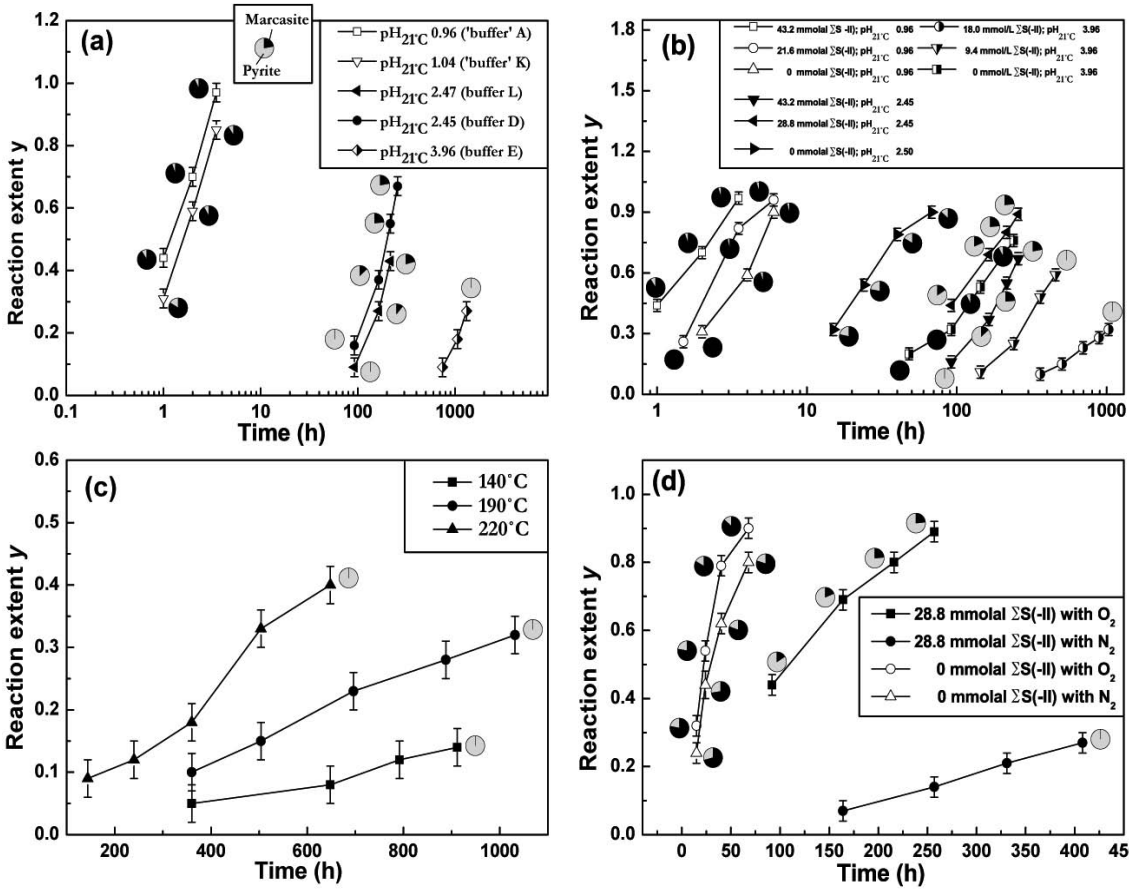

FIGURE 3. Reaction extent vs. time plots. The mineralogy of the product is shown as pie charts; only one chart is plotted along curves where only one product mineral was observed. (**a**) Reactions at different pH and at 190 °C (from Table 3). (**b**) Reactions at $pH_{21°C}$ 0.96 ("buffer" A), 2.45 (buffer D), and 3.96 (buffer E) and at 190 °C with different ΣS(-II) concentrations (from Table 4). (**c**) Reactions at $pH_{21°C}$ 3.96 and at different temperatures (from Table 5). (**d**) Reactions under different reaction atmosphere (with air gap or with N_2) at $pH_{21°C}$ 2.45/2.50 and at 190 °C with or without external S(-II) (Table 6). The true data points with error bars (i.e., ±3%; 3σ) for reaction extent y (i.e., weight fraction of product Fe disulfide) are plotted in all figures.

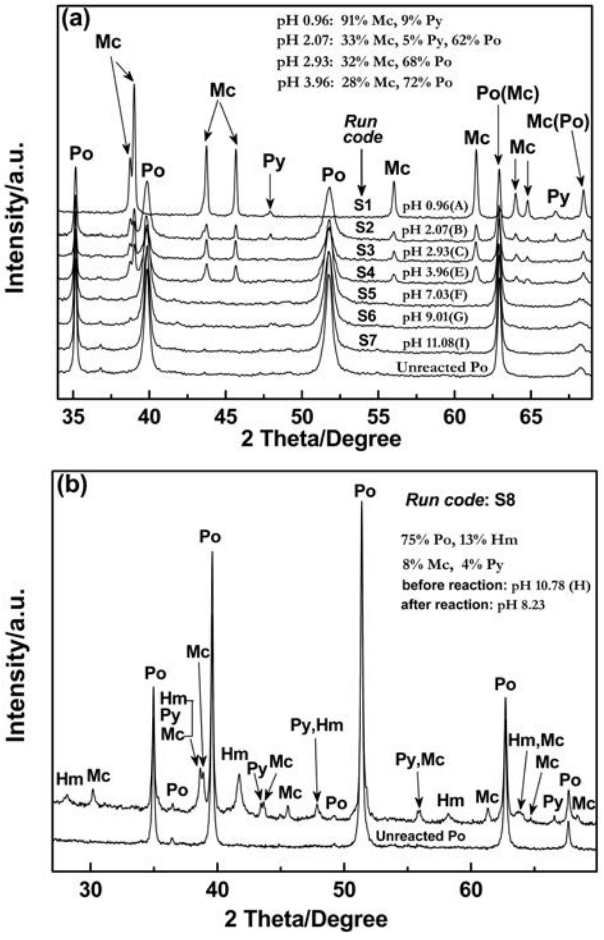

FIGURE 4. XRD patterns of products from replacement of pyrrhotite by Fe disulfide in the absence of external S(-II) under different $pH_{21°C}$ conditions. (**a**) Pyrrhotite (400–1000 μm pyrrhotite; 42.0 mg) replacement by Fe disulfide at 125 °C and different pH for 7 days. (**b**) Pyrrhotite (20–38 μm; 42.0 mg) replacement by Fe disulfide at 125 °C and $pH_{21°C}$ 10.78 for 28 days. The wt% of each mineral phase is given in **a** and **b** (also refer to Table 2). Buffers codes given in brackets used in this part of work are presented in Table 1. Errors for wt% are around ±3%. Mc = Marcasite; Py = Pyrite; Po = Pyrrhotite; Hm = Hematite.

that marcasite formation was favored if no external S(-II) source was introduced (Fig. 3b; Table 4). Hematite (Fe_2O_3, identified by XRD) was observed as a by-product only in some experiments where no external S(-II) was added. For example, hematite precipitated on the PTFE liners at $pH_{21°C}$ 3.96 (run S4 in Table 2 and Fig. 4a; note that no hematite was collected with pyrrhotite for XRD analysis), and on the pyrrhotite surface under basic conditions ($pH_{21°C}$ 10.78; run S8; Table 2 and Fig. 4b). At $pH_{21°C}$ 0.96, marcasite was always the predominant product and its formation was independent of S(-II) availability (Fig. 3b; Table 4).

The effect of ΣS(-II) concentrations on reaction rates was studied at $pH_{21°C}$ 0.96, $pH_{21°C}$ 2.45/2.50, and $pH_{21°C}$ 3.96 (Fig. 3b; Table 4). The overall reaction rate increased with decreasing ΣS(-II) concentration at $pH_{21°C}$ 2.45/2.50 and 3.96. For example, at $pH_{21°C}$ 2.45, 37(4) wt% FeS_2 [5(3) wt% Mc + 32(3) wt% Py] was obtained after 164 h from the experiment with 43.2 mmolal ΣS(-II) (run N8; Table 4), while 69(4) wt% FeS_2 [13(3) wt% Mc + 56(3) wt% Py] was produced over the same time from run P8 (Table 4) with 28.8 mmolal ΣS(-II). In contrast to $pH_{21°C}$ 2.45/2.50 and 3.96, the rate of the overall reaction giving mainly marcasite increased with increasing ΣS(-II) concentration at $pH_{21°C}$ 0.96 (Fig. 3b).

Note that an Fe phosphate precipitate was detected by XRD in the reaction products at low ΣS(-II) concentration (i.e., 7.2 mmolal) and at $pH_{21°C}$ 2.45 when a phosphate buffer was used (run M3; Buffer D; Table 2). In comparison, at higher ΣS(-II) concentrations and at different pH values with various phosphate buffers, no phosphates were detected by XRD or SEM-EDS (e.g., runs M7, M7-1, M13, and M17; Table 2).

The effect of temperature

The effect of temperature on the transformation rate was studied at $pH_{21°C}$ 3.96 and in the temperature range of 140–220 °C with 18 mmolal ΣS(-II) (Table 5; Fig. 3c). The rate of replacement increased with increasing temperature.

It is important to note that the hydrolysis rate of TTA to form S(-II) was effectively constant over the temperature range, so the above results truly reflect the effect of temperature on the replacement reaction rate. Since the pH_T of the acetate buffer used to probe this temperature effect increases slightly with temperature (cf. runs M8 and M16; Table 2), the reactions at "fixed" pH_T are expected to occur more rapidly with temperature than obtained experimentally, as reaction rates dropped with increasing pH.

The effect of oxygen availability

At $pH_{21°C}$ 0.96 and 190 °C under anaerobic condition (run M19; Table 2), 92(3) wt% marcasite and 8(3) wt% pyrite were obtained after 24 h, similar to the reaction products obtained in an experiment performed in the presence of oxygen (from the air gap; e.g., run M18; Table 2). The oxygen availability showed an insignificant effect on the rate of transformation at $pH_{21°C}$ 0.96; a similar weight percent of marcasite was obtained over the same reaction time in the presence of oxygen or N_2 (cf. runs M20 and M21; Table 2). At $pH_{21°C}$ 2.45/2.50 and 190 °C under N_2, pyrite formed in the presence of 28.8 mmolal ΣS(-II) (runs R1–R4; Table 6), while marcasite was the principal product formed in the absence of external S(-II) (runs R5–R8; Table 6; Fig. 3d). These products were similar to those obtained in experiments with oxygen (runs P7–P14; Table 6), with the difference that minor marcasite was observed in the experiments with external S(-II) and with oxygen but not under anaerobic conditions (runs R1–R4; Table 6; Fig. 3d). The main difference was that the overall reaction with external S(-II) (i.e., ~28.8 mmolal) occurred more rapidly in the presence of oxygen at $pH_{21°C}$ 2.45, while the oxygen availability did not affect the reaction rate significantly if no S(-II) was added at $pH_{21°C}$ 2.50 (Fig. 3d). At $pH_{21°C}$ 3.96, no reaction was detected by XRD in experiments after 984 h under N_2 and in the presence of 28.8 mmolal ΣS(-II) (run M25; Table 2), compared to 29(3) wt% pyrite formed from an experiment with oxygen under otherwise identical conditions (run M26; Table 2). In the absence of external S(-II) and at $pH_{21°C}$ 3.96, more marcasite was obtained from experiments with oxygen than with N_2 over the same reaction time (run M28 in Table 2 vs. run S4 in Table 2 and Fig. 4a).

TABLE 4. Effect of external ΣS(-II) concentration on pyrrhotite to Fe disulfide reaction at 190 °C*

$pH_{21°C}$ 0.96/$pH_{190°C}$ 1.02 (A) 60.0 mg TAA i.e., ~43.2 mmolal ΣS(-II) 32.0 mg pyrrhotite			$pH_{21°C}$ 0.96/$pH_{190°C}$ 1.02 (A) 30.0 mg TAA i.e., ~21.6 mmolal ΣS(-II) 32.0 mg pyrrhotite			$pH_{21°C}$ 0.96/$pH_{190°C}$ 1.02 (A) no TAA i.e., 0 mmolal ΣS(-II) 32.0 mg pyrrhotite		
Run code	Time (h)	Mc, Py (wt%)	Run code	Time (h)	Mc, Py (wt%)	Run code	Time (h)	Mc, Py (wt%)
N1	1	40, 4	P1	1.5	26, 0	P4	2	31, 0
N2	2	66, 4	P2	3.5	79, 3	P5	4	56, 3
N3	3.5	90, 7	P3	6	91, 5	P6	6	86, 4
$pH_{21°C}$ 2.45/$pH_{190°C}$ 3.28 (D) 60.0 mg TAA i.e., ~43.2 mmolal ΣS(-II) 32.0 mg pyrrhotite			$pH_{21°C}$ 2.45/$pH_{190°C}$ 3.28 (D) 40.0 mg TAA i.e., ~28.8 mmolal ΣS(-II) 32.0 mg pyrrhotite			$pH_{21°C}$ 2.50‡/$pH_{190°C}$ 2.56 (J) no TAA i.e., 0 mmolal ΣS(-II) 32.0 mg pyrrhotite		
N7	92	0, 16	P7	92	7, 37	P11	15	25, 7
N8	164	5, 32	P8†	164	13, 56	P12	24	42, 12
N9	216	13, 42	P9	216	19, 61	P13	40	66, 13
N10	257	15, 52	P10	257	21, 68	P14	68	78, 12
$pH_{21°C}$ 3.96/$pH_{190°C}$ 4.53 (E) 25.0 mg TAA i.e., ~18.0 mmolal ΣS(-II) 20.0 mg pyrrhotite			$pH_{21°C}$ 3.96/$pH_{190°C}$ 4.53 (E) 13.0 mg TAA i.e., ~9.4 mmolal ΣS(-II) 20.0 mg pyrrhotite			$pH_{21°C}$ 3.96/$pH_{190°C}$ 4.53 (E) (E) no TAA i.e., 0 mmolal ΣS(-II) 20.0 mg pyrrhotite		
P15	360	10	P20	144	11	P24	48	20, 0
P16	504	15	P21	240	25	P25	92	32, 0
P17	696	23	P22	360	48	P26	144	49, 4
P18	888	28	P23	456	59	P27	240	70, 6
P19	1032	32						

* 125–150 μm pyrrhotite grains were used in experiments throughout this table; errors of the wt% are around ±3%; Mc = Marcasite; Py = Pyrite. Buffer codes were also given in the table.
† Mass of reaction products: 31.9 mg.
‡ The $pH_{21°C}$ 2.45 phosphate buffer (E) was not used for this group of experiments with no external S(-II) added, since there were significant amounts of Fe phosphates precipitation together with marcasite.

TABLE 5. Reaction extent vs. time at $pH_{21°C}$ 3.96 (buffer D) and at different temperatures

140 °C/$pH_{140°C}$ 4.29			190 °C/$pH_{190°C}$ 4.53			220 °C/$pH_{220°C}$ 4.70		
Run code	Time (day)	Py (wt%)	Run code	Time (day)	Py (wt%)	Run code	Time (day)	Py (wt%)
Q1	15	0	P15	15	10	Q6	6	9
Q2	21	5	P16	21	15	Q7	10	12
Q3	27	8	P17	29	23	Q8	15	18
Q4	33	12	P18	37	28	Q9	21	33
Q5	38	14	P19	43	32	Q10	27	40

Notes: 20.0 mg pyrrhotite between 125–150 μm was used in each experimental run; 25.0 mg thioacetamide [equivalent to 18 mmolal ΣS(-II)] was introduced into each run. Py = pyrite; errors of the wt% of the product are around ±3%.

TABLE 6. Effect of reaction atmosphere on pyrrhotite to Fe disulfide reaction at 190 °C

$pH_{21°C}$ 2.45/$pH_{190°C}$ 3.28 (D) 40.0 mg TAA i.e., ~28.8 mmolal ΣS(-II) 32.0 mg pyrrhotite air applied			$pH_{21°C}$ 2.45/$pH_{190°C}$ 3.28 (D) 40.0 mg TAA i.e., ~28.8 mmolal ΣS(-II) 32.0 mg pyrrhotite N_2 applied			$pH_{21°C}$ 2.5/$pH_{190°C}$ 2.56 (J) no TAA i.e., 0 mmolal ΣS(-II) 32.0 mg pyrrhotite N_2 applied			$pH_{21°C}$ 2.50/$pH_{190°C}$ 2.56 (J) no TAA i.e., 0 mmolal ΣS(-II) 32.0 mg pyrrhotite; air applied		
Run code	Time (h)	Mc, Py (wt%)	Run code	Time (h)	Py (wt%)	Run code	Time (h)	Mc, Py (wt%)	Run code	Time (h)	Mc, Py (wt%)
P7	92	7, 37	R1	164	7	R5	15	17, 7	P11	15	25, 7
P8	164	13, 56	R2	257	14	R6	24	32, 12	P12	24	42, 12
P9	216	19, 61	R3	331	21	R7	40	50, 12	P13	40	66, 13
P10	257	21, 68	R4	408	27	R8	68	64, 16	P14	68	78, 12

Notes: 125–150 μm pyrrhotite was used in experiments throughout this table; errors of the wt% are around ±3%. Mc = Marcasite; Py = Pyrite.

The textures

The textures of the reaction products were found to vary strongly depending on experimental conditions, with pH and availability of external S(-II) showing the most pronounced effects.

At very low $pH_{21°C}$ with additional S(-II) [e.g., $pH_{21°C}$ 0.96; 7.2 mmolal ΣS(-II)], marcasite was the predominant product. Backscattered electron images of the polished cross section of the products revealed that pyrrhotite dissolved, leaving only marcasite as an outer rim after 100% reaction (Fig. 5a). The marcasite itself showed a micro-porous texture with pores <1 μm in size (Fig. 5b) and preserved the outer shape of the pyrrhotite (Fig. 5c). Nano-sized euhedral marcasite crystals formed only on the surface of the marcasite grains; these nanocrystals show coherent orientation (top inset in Fig. 5c). EBSD pole figures (e.g., Figs. 6a and 6b) from two partially replaced pyrrhotite grains at $pH_{21°C}$ 0.96 and at 190 °C for 2 h (run N2; Table 3) showed that both parent pyrrhotite and the product marcasite were crystallographically related with: $\{10\bar{1}0\}_{po}\|\{010\}_{mc}$, $\{0001\}_{po}\|\{100\}_{mc}$, $\{1\bar{2}10\}_{po}\|\{001\}_{mc}$. This preservation of crystallographic relationship is consistent with the observations by Fleet (1978) on natural assemblages.

At $pH_{21°C}$ 2.45, the pyrrhotite to pyrite (primary product) reaction in the presence of external S(-II) (Tables 2 and 3) showed a sharp reaction interface between pyrrhotite and the product phase (Fig. 5d), with sub-micrometer sized pores existing in the outer pyrite rim. Pyrite overgrowth was observed as well as precipitation of minor amounts of pyrite on the PTFE liners. Randomly oriented euhedral pyrite crystals of the order of ~100

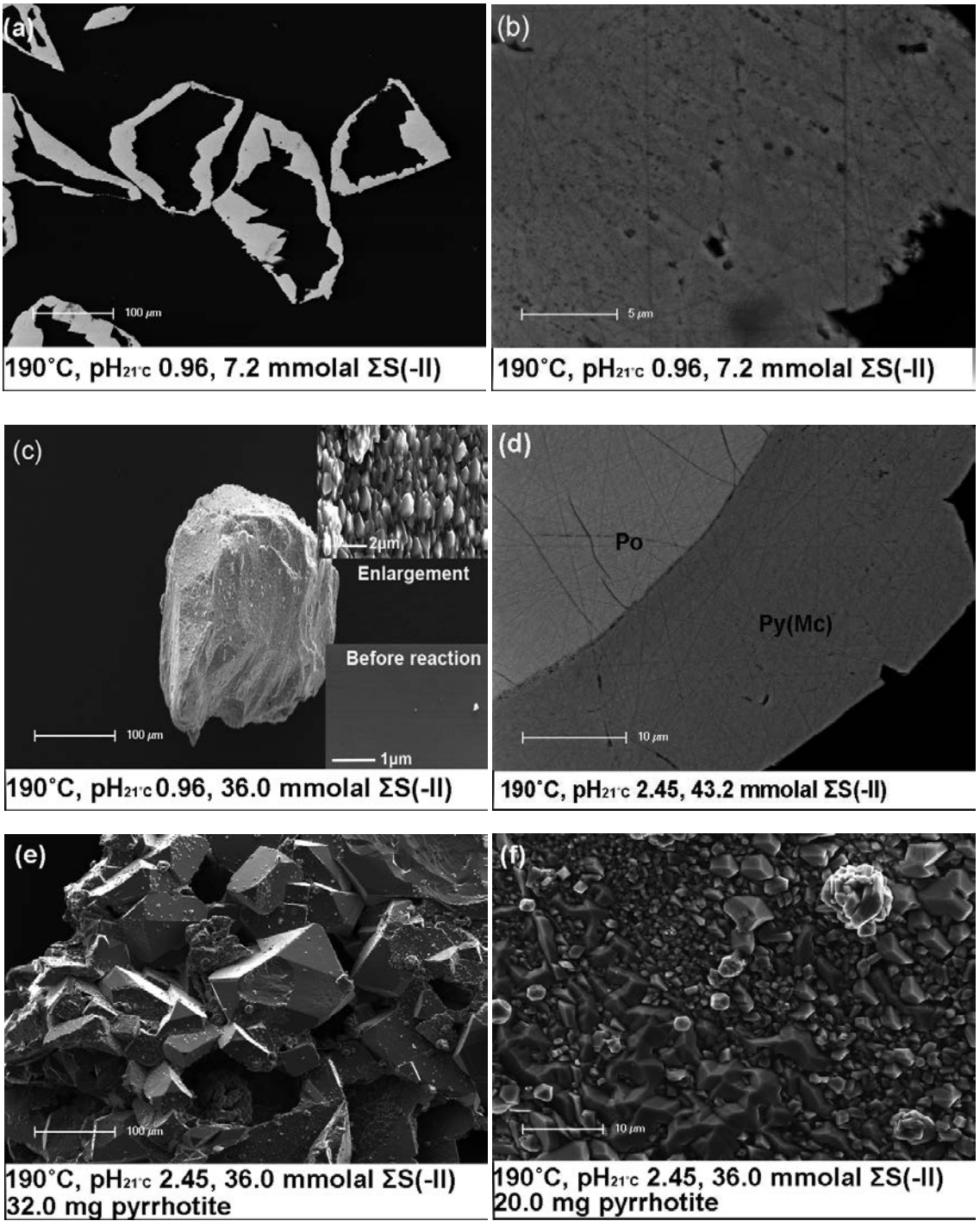

FIGURE 5. Backscattered electron (BSE) and secondary electron (SE) images of reaction products. (**a**) BSE image of polished cross section of reaction product (marcasite) from experiment M2 (Table 2). (**b**) Enlargement of the rim in **a**. (**c**) Surface morphology of the surface of reaction products in M6 (Table 2), enlargement of the surface, and pyrrhotite surface before reaction (**d**). BSE of polished cross section of product from N8 in Table 3. (**e**) Surface morphology of reaction products in run M7 (Table 2). (**f**) Surface morphology of reaction products from run M7-1 (Table 2). Po = Pyrrhotite; Mc = Marcasite; Py = Pyrite.

(continued on next page)

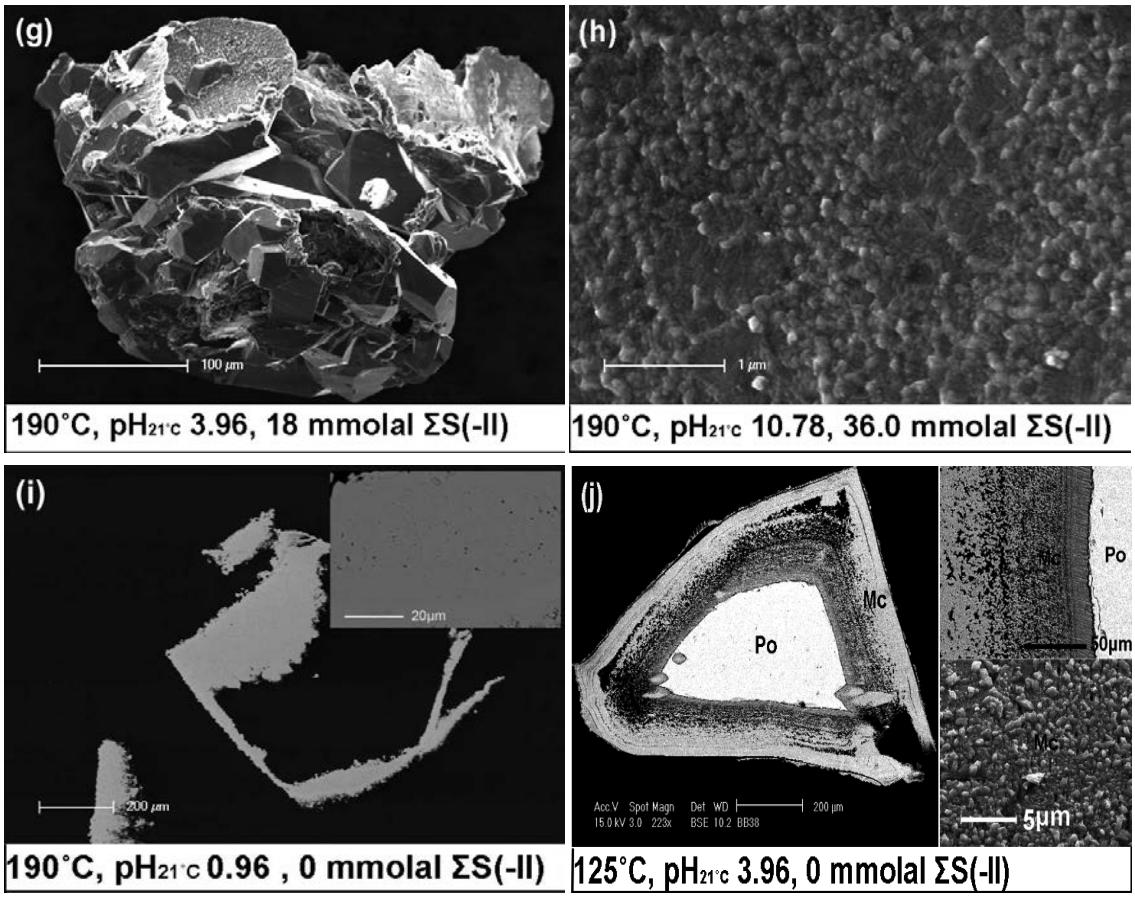

FIGURE 5.—*CONTINUED* (**g**) Surface morphology of reaction product (pyrite) from run P19 (Table 5). (**h**) SE image of the surface morphology of reaction products from run M27 (Table 2). (**i**) Marcasite (and minor pyrite) replacing pyrrhotite after 100% reaction [93(3) wt% Mc + 7(3) wt% Py] in the presence of air gap. (**j**) A BSE image of polished cross section of pyrrhotite to marcasite reaction at $pH_{21°C}$ 3.96 without external S(-II) and in the presence of air gap (left image), showing large gaps and cracks of secondary marcasite (400–1000 μm pyrrhotite grains; 42 days), enlargement of the reaction interface (top right), and surface morphology of the product marcasite (bottom right). Po = Pyrrhotite; Mc = Marcasite; Py = Pyrite.

μm grew on the pyrrhotite surface when larger quantities of pyrrhotite were used (run M7 vs. run M7-1; Table 2; cf. Figs. 5e and 5f). At $pH_{21°C}$ 3.96, euhedral pyrite crystals also formed on the pyrrhotite surface (Fig. 5g). In contrast, at $pH_{21°C}$ 10.78, the pyrite on pyrrhotite surface showed an anhedral nature (Fig. 5h).

The euhedral pyrite overgrowth did not show any preferential orientation (e.g., Fig. 5e). EBSD analysis on reacted pyrrhotite grains where no apparent overgrowth of pyrite was observed (M7-1; Table 2; Fig. 5f) showed that the parent pyrrhotite, similar to the EBSD analysis in Figure 6, had a coherent crystallographic orientation, while the product pyrite consisted of randomly oriented crystals >10 μm in size (Figs. 7a and 7b). According to Fleet (1970, 1978), if pyrrhotite and pyrite are crystallographically intergrown, the pyrrhotite $\{22\bar{4}\bar{5}\}$ planes (parallel to marcasite {101}) should be parallel to pyrite {001} (sub-parallel to marcasite {101}). However, we did not observe such a relationship between pyrrhotite and pyrite in this work (Fig. 7b).

Marcasite formed at $pH_{21°C}$ <3 in the absence of external S(-II) had a similar texture to that formed at $pH_{21°C}$ 0.96 with an external S(-II) source (Figs. 5a, 5b, and 5i), but marcasite formed at $pH_{21°C}$ >3 without any S(-II) showed a distinctly different texture. In the latter case, marcasite exhibited a layer texture, with cracks and micro-pores within the marcasite and sometimes a thin gap at the reaction interface (e.g., Figs. 5j and 6c). The marcasite crystallites are similar in size to those obtained at lower $pH_{21°C}$ (cf. Figs. 5c and 5j), but are anhedral in shape. In contrast, there was a large gap between the parent pyrrhotite and the secondary marcasite formed at $pH_{21°C}$ 0.96 with or without external S(-II) and at $pH_{21°C}$ 2.50 without additional S(-II) (similar textures as shown in Fig. 6a). The marcasite formed at $pH_{21°C}$ 0.96 (three reacted grains from M20; Table 2) and 2.50 (two reacted grains from run P13; Table 4) in the absence of any external S(-II), showed previously noted preferred orientation controlled by the orientation of the parent pyrrhotite crystal. In comparison, at $pH_{21°C}$ 3.96 with no external S(-II) (two reacted grains from run P25 in Table 4 and run S4 in Table 2 and Fig. 4a, respectively), there was no consistent crystallographic relationship between parent pyrrhotite and product marcasite, and the marcasite orientation was random (e.g., Fig. 6d). SEM images revealed that some of the marcasite crystals formed at $pH_{21°C}$ 3.96 displayed

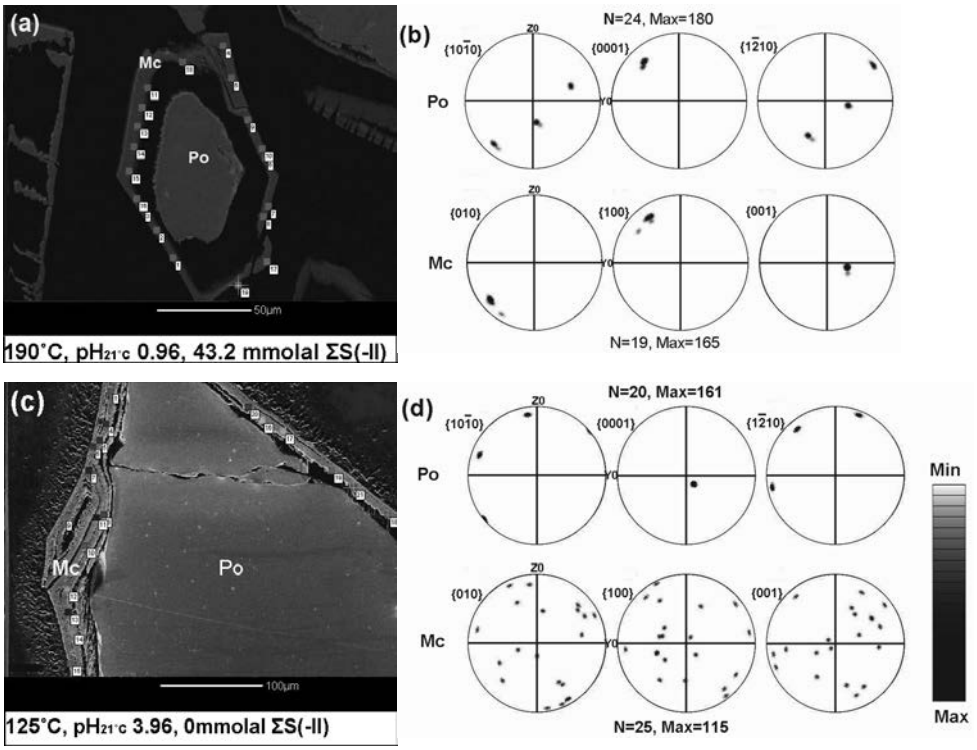

Figure 6. EBSD analyses of parent pyrrhotite and marcasite rim formed at $pH_{21°C}$ 0.96 (**a** and **b**) and at $pH_{21°C}$ 3.96 (**c** and **d**). (**a**) SE image of pyrrhotite being replaced by marcasite at $pH_{21°C}$ 0.96 (buffer A) and 190 °C for 2 h (run N2 in Table 3). (**b**) Contoured poles figures for pyrrhotite (based on N = 24 point analyses) and marcasite (based on N = 19 point analyses), which show that there is a certain crystallographic relationship between the parent pyrrhotite and the product marcasite. (**c**) SE image of pyrrhotite being replaced by marcasite at $pH_{21°C}$ 3.96 (buffer E) in the presence of oxygen (run S4 in Table 2 and Fig. 4a). (**d**) Contoured pole figures for pyrrhotite (based on N = 20 points) and marcasite (based on N = 25 points), which shows no crystallographic relationship between two minerals. Contoured pole figures are used here to show the data more clearly. Linear scale bar in **d** also applied to **b**. The EBSD data was obtained on the HKL EBSD system. Mc = Marcasite; Po = Pyrrhotite.

an acicular habit at the interface with pyrrhotite; these acicular crystals often grow perpendicular to the dissolution surface (Fig. 5j top inset).

Discussion

Mechanism of the replacement reaction: solid-state or dissolution-reprecipitation replacement reaction?

This experimental study shows that the replacement of pyrrhotite by marcasite and pyrite occurred readily under mild hydrothermal conditions and that the nature of the products and their textures were controlled principally by fluid composition. Marcasite replaced pyrrhotite either as a polycrystalline, fine-grained product lacking a particular crystallographic orientation with the parent pyrrhotite, or as aggregates of nanocrystals that had a homogeneous crystallographic orientation reflecting the crystal structure of the parent pyrrhotite. In contrast, pyrite replacing pyrrhotite consisted of relatively coarse aggregates of randomly oriented pyrite crystals.

Murowchick (1992) proposed that the preservation of crystallographic relationship implied a solid-state reaction, as opposed to the dissolution-reprecipitation mechanism he suggested in cases where crystallographic orientation was not preserved. However, the textural and other evidences from our experiments clearly point to an interface coupled dissolution-reprecipitation reaction, rather than solid-state transformation being responsible for pyrrhotite replacement under all investigated conditions. The following observations are consistent with an interface coupled dissolution-reprecipitation mechanism. (1) Sharp reaction fronts between pyrrhotite and pyrite were observed in experiments for both pyrrhotite to pyrite (e.g., Fig. 5d) and pyrrhotite to marcasite (Fig. 5j) transformations. In contrast, processes driven by solid-state diffusion result in structural and chemical gradients (e.g., Geisler et al. 2003; Watson and Cherniak 1997). (2) Euhedral pyrite crystals were observed in our experiments under certain conditions (e.g., $pH_{21°C}$ 2.45; 32.0 mg pyrrhotite; Fig. 5e), indicating that pyrite grew from the solution. (3) The control from solution pH and ΣS(-II) concentration on the formation of pyrite or marcasite as dominant Fe disulfide was consistent with their precipitation directly from solution. (4) The effects of solution composition on the overall transformation rates were consistent with a dissolution-reprecipitation mechanism, not with solid-state diffusion. For example, the reaction rate was pH dependent, which is not expected for a solid-state reaction, but can be fully interpreted as a fluid-chemistry-mediated dissolution-reprecipitation mineral replacement reaction (e.g., Xia et al. 2009a, 2009b). In addition, the slowing down of the reaction

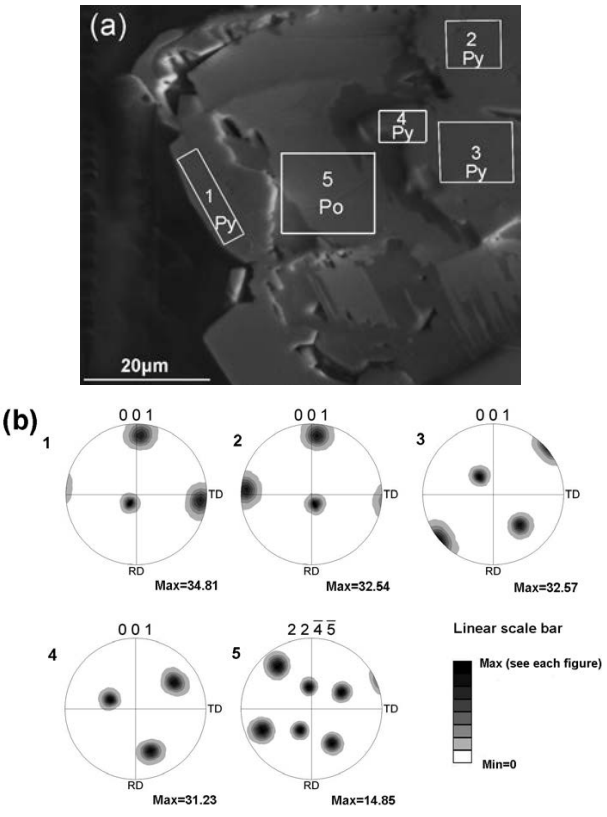

Figure 7. EBSD analyses (mapping) of pyrrhotite and secondary pyrite (with minor marcasite) from experiment M7-1 (Table 2). (**a**) SE image of the reacted sample; (**b**) {001} pole figures for pyrite indicating that different pyrite crystals have different orientations, and $\{22\bar{4}\bar{5}\}$ pole figures for pyrrhotite. The numbers in **b** correspond to the pyrite and pyrrhotite area in **a**.

upon increasing ΣS(-II) concentration under most pH conditions (except $pH_{21°C}$ 0.96) can be explained in the context of dissolution/reprecipitation as reflecting lower solubility of pyrrhotite; however, it is inconsistent with sulfidation of pyrrhotite via solid-state diffusion of S atoms, since reaction rate would be expected to increase with ΣS(-II) concentrations. (5) At $pH_{21°C}$ 0.96 after 100% transformation of pyrrhotite to marcasite, the marcasite existed as an outer rim and pyrrhotite had disappeared, leaving a large hollow core. In the case of solid-state reaction suggested by Murowchick (1992), the Fe should be "leached out" uniformly from the pyrrhotite, producing porous rather than hollow grains. (6) The presence of porosity in all the products is consistent with a dissolution-reprecipitation process, allowing for solute transport to and from the reaction front (reviews in Putnis 2002, 2009). All the transformation products were finely cracked and micro-porous (e.g., Figs. 5b and 5d). The presence of porosity is necessary for the development of replacement via coupled dissolution/reprecipitation, but it is not a distinguishing feature. For example, Murowchick (1992) showed that marcasite annealed at 500 °C for 48 h under dry conditions and under vacuum transformed via a solid-state process to porous pyrite; in this case the porosity was associated with a volume change of –2.6%.

Controls on the mineralogy and textures of the replacement reaction

Pyrite or marcasite? In the context of dissolution-reprecipitation replacement reaction, the formation of Fe disulfide requires the dissolution of the parent pyrrhotite to liberate Fe and S [in the absence of an external S(-II)] necessary for pyrite/marcasite precipitation. Under acidic conditions, the dissolution reaction can be written for example as

$$Fe_8S_{9(po)} + 16H^+_{aq} = 8Fe^{2+}_{aq} + 8H_2S_{aq} + S^0. \quad (6)$$

Murowchick (1992) proposed that both pyrite and marcasite formed from pyrrhotite following the O_2-pathway via polysulfides (Eq. 3a), and that nucleation of marcasite instead of pyrite was favored at $pH_{21°C}$ <5 because of the presence of fully protonated polysulfides in solution (i.e., neutral sulfanes; Murowchick and Barnes 1986; Eq. 4).

Although the polysulfide route may explain marcasite being more important with decreasing pH in experiments performed with external S(-II) (e.g., Table 3), it cannot explain why marcasite was dominant under both acidic and basic conditions in experiments with no external S(-II) (Table 4; Figs. 4a and 4b) and neither can it explain why significant weight percent of marcasite and pyrite were obtained under near anaerobic conditions, where there was hardly any oxygen (or other oxidants) to produce polysulfides.

We propose that the saturation level of pyrite/marcasite rather than polysulfides speciation played a critical role in determining, which Fe disulfide precipitated. Marcasite was dominant at $pH_{21°C}$ 0.96, independently of the concentration of external S(-II) in solution. At such low pH and assuming that all pyrrhotite dissolves into solution without any precipitation of Fe disulfide, the calculated maximum supersaturation ratio with respect to marcasite (and pyrite) is below 1000 (Figs. 8a and 8b). Since unreacted pyrrhotite was observed after hydrothermal reactions in most cases at $pH_{21°C}$ 0.96, marcasite precipitation probably started at a lower saturation state (≤10). Marcasite nucleation is favored in the presence of pyrrhotite due to the similarity of the S lattices in both minerals. The role of pyrrhotite in promoting marcasite (epitaxial) nucleation is confirmed by the preservation of crystallographic orientation at $pH_{21°C}$ <3 and the fact that marcasite formed only on pyrrhotite grains, not on other parts of the autoclaves. In contrast, pyrite nucleation requires a supersaturation ratio as high as 10^{11}–10^{14} at low temperatures (25–55 °C; Harmandas et al. 1998; Rickard et al. 2007).

At $pH_{21°C}$ >2, marcasite formed only in the absence of external S(-II), while pyrite became dominant in the presence of external S(-II). The predominance of pyrite at high ΣS(-II) concentrations is attributed to the increase in FeS_2 supersaturation ratio enabling pyrite nucleation (Fig. 8c vs. Fig. 8d; Fig. 8e vs. Fig. 8f). For example, at 190 °C and $pH_{21°C}$ 2.45 (i.e., $pH_{190°C}$ 3.28) with only 1.0 mg pyrrhotite dissolved into solution, the supersaturation ratio of pyrite in the bulk solution reached ~10^5 with 43.2 mmolal ΣS(-II), but only <10^2 with 0 mmolal ΣS(-II).

The effect of external S(-II) on supersaturation level and hence on pyrite nucleation is also further illustrated by an experiment conducted at $pH_{21°C}$ 0.96 with a high ΣS(-II) concentration of 72.0 mmolal (run M10; Table 2), that yielded 18(3) wt% pyrite

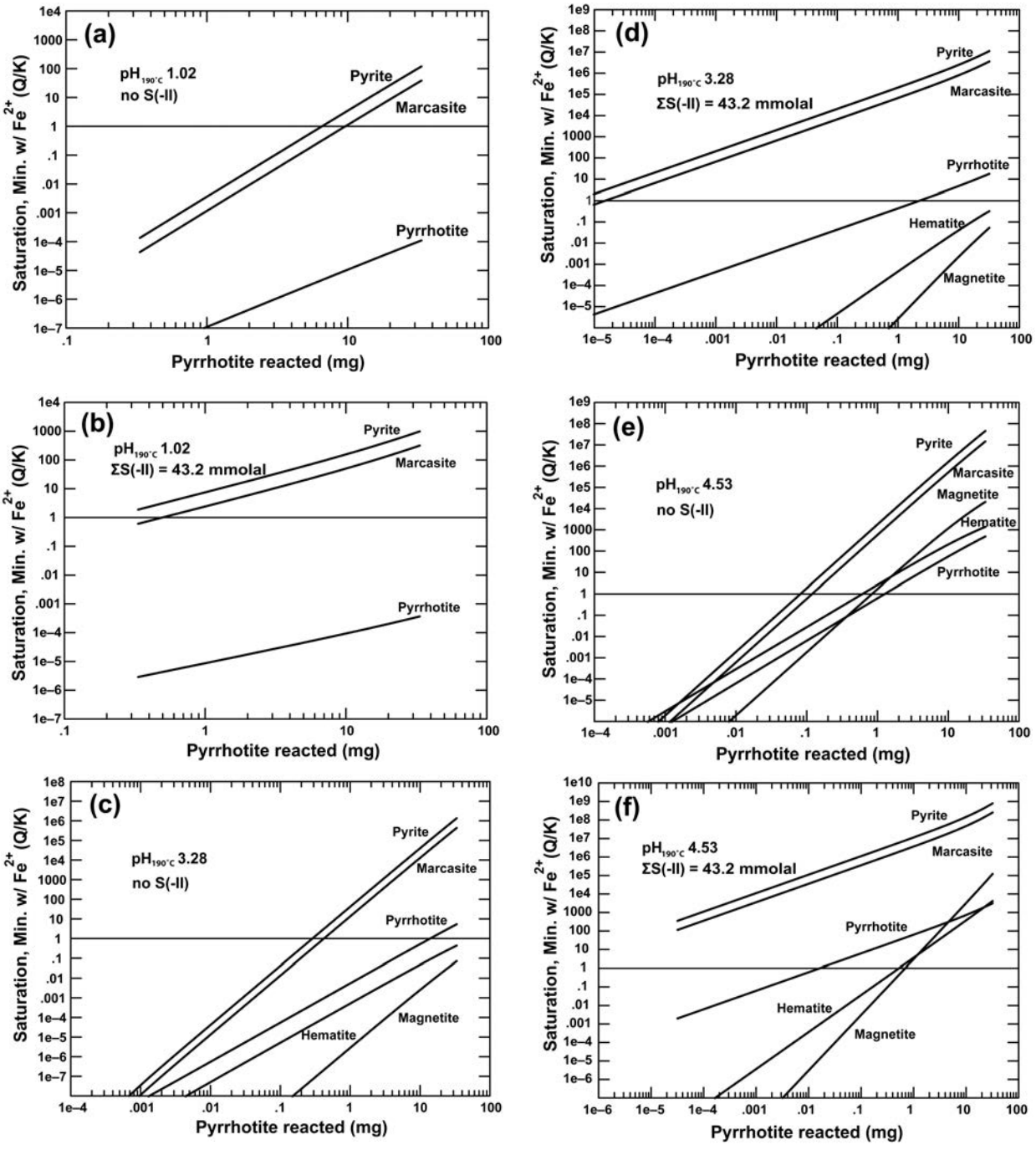

FIGURE 8. Fe mineral saturation indices vs. mass of pyrrhotite dissolved (pyrrhotite experimental load of 32.0 mg) at 190 °C for $pH_{190°C}$ 1.02 (**a** and **b**), $pH_{190°C}$ 3.28 (**c** and **d**), and $pH_{190°C}$ 4.53 (**e** and **f**) with no external S(-II) or with ΣS(-II) = 43.2 mmolal (equivalent to 60.0 mg thioacetamide). These diagrams were modeled by Geochemist's Workbench REACT program and explicitly take into account the buffer compositions (e.g., Fe-complexing via acetate; ionic strength). The amount of oxygen (~5.1×10^{-5} mol) in the autoclave is included into the modeling. The curves above the horizontal line (Q/K = 1) in all figures indicate that the solutions are supersaturated with respect to each mineral, while curves below the line (Q/K = 1) means that solutions are undersaturated with respect to the corresponding minerals. In these calculations no minerals were allowed to precipitate. pH was fixed to the value shown in each diagram.

and 82(3) wt% marcasite. This represents a higher proportion of pyrite compared to <10(3) wt% pyrite obtained in the other $pH_{21°C}$ 0.96 experiments conducted at lower ΣS(-II) concentrations [e.g., 7(3) wt% pyrite from run M2 with 7.2 mmol ΣS(-II); Table 2].

The overall reaction. Murowchick (1992) proposed a polysulfide reaction route for pyrite and marcasite formation via dissolution/reprecipitation mechanism from pyrrhotite (i.e., O_2-pathway; Eq. 3a), and assumed S conservation through re-

action. For the composition of pyrrhotite used in this work, the proposed resulting overall reaction can be written as

$$2Fe_8S_9 + 14H^+ + {}^7/_2O_{2aq} = 9FeS_{2s} + 7Fe^{2+}_{aq} + 7H_2O. \quad (3b)$$

Volume decrease: 31.3% (pyrite) and 28.7% (marcasite)

We argue here that Equation 3b cannot fully explain the overall reaction in our experiments. Instead, the main difference in overall reaction is that the reactions producing mainly marcasite were conservative with respect to S (O_2 and Fe-loss pathways; Eqs. 3b and 1b), while those producing mainly pyrite tended to conserve Fe (O_2 and H_2S pathways; Eqs. 3c and 2b; refer to discussions in the following text).

The O_2-pathway requires an external oxidant to form polysulfides. However, experiments under N_2 demonstrated that a significant weight percent of pyrite/marcasite was obtained even in the absence of oxygen. Moreover, Equation 3b cannot fully account for reactions performed in the presence of air, because not enough O_2 was present to explain the amount of FeS_2 formed. For example, in run M18 (Table 2), the oxygen present in the air gap and solution (total oxygen: ~5.1×10^{-5} mol) could lead to the formation of ~15.7 mg FeS_2 according to Equation 3b, compared to 20.6 mg FeS_2 obtained in this run. Indeed, a similar amount of FeS_2 (18.9 mg) formed under N_2 (run M19; Table 2). A similar situation was found for the formation of pyrite. The amount of oxygen in the closed system would yield ~15.7 mg FeS_2 via Equation 3b, but one experiment (run P8; Table 4) produced as much as 22.0(1.3) mg FeS_2.

For the pyrrhotite composition (converted into Fe_8S_9) used in this study, the Fe-loss pathway is written as

$$2Fe_8S_{9(po)} + 14H^+ = 9FeS_{2(s)} + 7Fe^{2+}_{aq} + 7H_{2(g)}. \quad (1b)$$

Volume decrease: 31.3% (pyrite) and 28.7% (marcasite)

The O_2 (Eq. 3b) and Fe-loss pathways (Eq. 1b) both result in a strong volume decrease and solubilization of Fe, features observed in the marcasite replacement experiments. In run M18 (Table 2), for example, 53.0 mg pyrrhotite were replaced by 20.6 mg FeS_2; this reflects a ~62% volume decrease, indicating a large Fe [and some S(-II)] loss to the solution. Fe-loss to solution was confirmed by solution ICPMS analysis of the post reaction fluid from run M18, showing that it contained 1183(22) ppm Fe, which is consistent with ~1221 ppm Fe calculated based on Equations 3b or 1b. Note that the ~1221 ppm Fe consists of two contributions: first, Fe released via the formation of 20.6 mg FeS_2 from 28.1 mg of pyrrhotite according to Equations 3b or 1b, and second Fe released by the dissolution of 24.9 mg pyrrhotite (i.e., total 53.0 mg – reacted 28.1 mg) lost to solution without forming secondary minerals via Equation 6. Formation of marcasite under N_2 must proceed mainly following the Fe-loss pathway (i.e., Eq. 1b). The precipitation of hematite on the PTFE liners in experiments at $pH_{21°C}$ >3 without external S(-II) and in the presence of oxygen suggests that sufficient O_2 in the system [i.e., no reaction with S(-II)] eventually reacted with Fe^{2+}_{aq} released by the dissolution of pyrrhotite to form hematite.

In contrast to what was observed for marcasite, no extensive porosity formed during the replacement of pyrrhotite by pyrite, and the product pyrite contained only minor micro-pores (e.g., Fig. 5d). The mass of Fe-sulfide minerals was usually constant or slightly increased before and after reaction (e.g., N16 in Table 3 and P8 in Table 4). Hence, Equations 1b and 3b, which assume S immobility and a large mass loss, cannot account for pyrite formation. Instead, Fe appears to be poorly mobile under conditions in which pyrite formed. This assumption was confirmed by the solution analysis of Fe in run N16 (Table 3) at $pH_{21°C}$ 3.96 with 43.2 mmolal ΣS(-II), in which 8.7(9) mg pyrite was obtained. According to reactions 1b or 3b, 3.2(3) mg Fe^{2+}_{aq} corresponding to 173(16) ppm Fe in solution should be lost to solution; however, the solution contained only 42(1) ppm Fe (Table 3). The limited Fe mobility during pyrite formation is consistent with the requirement of high supersaturation levels identified above which explains the preferential formation of pyrite over marcasite. Assuming Fe immobility, the following overall reactions giving pyrite can be expressed as

$$Fe_8S_{9(po)} + 7H_2S_{aq} = 8FeS_{2(py)} + 7H_{2(g)}$$

(anoxic and acidic conditions) (2b)

$$2Fe_8S_{9(po)} + 14H_2S + 7O_{2aq} = 16FeS_{2(py)} + 14H_2O$$

(oxic and acidic conditions) (3c)

Volume increase for both reactions: 15.9%

The replacement of pyrrhotite by pyrite occurred more rapidly with oxygen than with N_2, suggesting that reaction mechanisms 2b and 3c are both viable. The oxic route appears kinetically more favorable, since reactions in the presence of external S(-II) appeared to occur more rapidly under oxic conditions (Fig. 3d). Note that even in the presence of O_2, the amount of available O_2 was insufficient to produce the obtained weight of pyrite via Equation 3c: the total amount of oxygen in the closed system was ~5.1×10^{-5} mol, accounting for the production of ~14.0 mg pyrite at most. Nevertheless, as much as 17.9(9) mg pyrite [22.0(1.3) mg of total FeS_2] was formed (run P8; Table 4).

Why does marcasite sometimes preserve the crystallographic orientation of the parent pyrrhotite? Marcasite preserved the crystallographic orientation of parent pyrrhotite only in experiments conducted at $pH_{21°C}$ 0.96 and $pH_{21°C}$ 2.50; at higher pH, marcasite displayed random orientation. In both cases, the individual marcasite crystals had sub-micrometer sizes. At low pH, the pyrrhotite dissolution rates are expected to be very fast initially, because the solutions are highly undersaturated with respect to pyrrhotite (Fig. 8). This results in the formation of a solution layer very rich in S and Fe near the surface of the dissolving pyrrhotite. This surface layer will rapidly become supersaturated with respect to marcasite, explaining the initial nucleation of numerous marcasite nanocrystals and the preservation of the outer shape of the pyrrhotite crystal. If the nucleation of the marcasite crystals occurs epitaxially on the pyrrhotite surface, the crystallographic orientation of the parent pyrrhotite will be preserved.

In contrast, at higher $pH_{21°C}$ (~4) nucleation was still fast (small marcasite crystallites), but did not happen epitaxially. We suggest that this is related to changes in the electrostatic properties of the pyrrhotite surface with increasing pH. The pH of point of zero charge (pH_{pzc}) for a synthetic pyrrhotite was determined by Widler and Seward (2002) to be 2.7 at

room temperature. The change of surface charge as a function of pH may therefore explain the change in nucleation of marcasite from epitaxial to random. At low pH, the positively charged pyrrhotite surface is a suitable receptor for sorption of the precursor aqueous species, a process followed by epitaxial nucleation. In contrast, at pH > pH_{pzc} the negatively charged surface does not favor sorption of these species, preventing epitaxial nucleation of marcasite.

Why are the textures obtained via replacement by pyrite different from those observed for the replacement by marcasite? Formation of marcasite appears to be controlled by fast nucleation, with grain sizes <1 μm. At $pH_{21°C}$ <3, nucleation initiates epitaxially on the surface of the dissolving pyrrhotite grain, leading to preservation of the outer shape of the pyrrhotite grain and of its crystallographic orientation. As the reaction progresses, however, further nucleation occurred mainly on the inside of the marcasite rim, and a large gap appeared between the pyrrhotite and the marcasite rim, eventually leaving a cavity within the marcasite grain (e.g., Fig. 5a). At $pH_{21°C}$ >3, nucleation occurred very close to the dissolution surface, but not epitaxially (Fig. 5j). In contrast, nucleation of pyrite was slow relative to its growth (Rickard and Luther 2007). Hence, the precipitation reaction was controlled by the growth of the pyrite crystals, which led to larger grain sizes. As pyrite nucleation was slow, it could occur relatively far away from the dissolving pyrrhotite surface (micrometer to centimeter), leading to overgrowth and pyrite precipitation on the PTFE liners. Hence, at a fundamental level, the different textures observed reflect the interplay between nucleation and growth of the replacing minerals.

Xia et al. (2009a) showed that in order for nanometer-scale pseudomorphism via interface-coupled dissolution/reprecipitation reaction to take place, the dissolution reaction needs to be rate-limiting relative to the precipitation (i.e., precipitation occurs much more rapidly than dissolution). At $pH_{21°C}$ >2 with additional S(-II), increasing ΣS(-II) concentration inhibited the dissolution of pyrrhotite (Eq. 6) but promoted the precipitation of Fe disulfide. This inverse dependence of reaction rate on the external ΣS(-II) concentration indicates that pyrrhotite dissolution was the rate-limiting step rather than pyrite precipitation, which is consistent with the fine replacement observed, for example, in Figure 5d.

Under very acidic conditions ($pH_{21°C}$ 0.96), the proposition that marcasite precipitation was the rate-limiting step is supported by increasing rates of marcasite formation with increasing concentration of ΣS(-II), which cannot be explained by the pyrrhotite dissolution being the rate-limiting step. If the pyrrhotite were rate-limiting at $pH_{21°C}$ 0.96, the increasing concentration of external ΣS(-II) would be expected to decrease the pyrrhotite dissolution and hence would slow down the overall reaction. The marcasite precipitation being the rate-limiting step explains the large gap between pyrrhotite and marcasite at $pH_{21°C}$ 0.96, and the fact that although the external shape and crystallographic orientation of the pyrrhotite grains was preserved, no internal feature was preserved under these conditions.

Complexity of mineral replacement reactions

This experimental study of the transformation of pyrrhotite to Fe disulfide illustrates the complexity of mineral replacement reactions following the interface coupled dissolution-reprecipitation mechanism. The nature of the products (marcasite or pyrite) depended upon competition between nucleation and growth, which in turn was controlled by the bulk solution chemistry, and in particular the saturation level with respect to the new phases, and the nature of the mineral surfaces available, whose states were controlled by reaction parameters such as pH.

Coupled dissolution-reprecipitation reactions can occur in a non-intuitive manner. For example, our results confirm the assumption of Murowchick (1992) that polycrystalline pyrite can form by replacing pyrrhotite without involving marcasite, despite the fact that the similarity in the sulfur lattice of marcasite and pyrrhotite suggests that marcasite should form instead (Fleet 1978). Our experiments also show that depending on solution compositions, marcasite can replace pyrrhotite with or without preserving the orientation of the pyrrhotite. Hence, in contrast to the assumption of Murowchick (1992), the preservation of the crystallographic orientation is not a distinguishing feature between dissolution-reprecipitation and solid-state reactions.

Importantly for the use of mineral textures to reconstruct ancient hydrothermal systems, this study shows that the presence of marcasite replacing pyrrhotite does not necessarily indicate low pH, but may instead reflect S(-II)-poor hydrothermal fluids. This is an example of reaction mechanism affecting the nature of the product. In another study involving replacement of one sulfide by another, Xia et al. (2009a) have shown how metastable violarite is the only sulfide to form from pentlandite over a wide range of pressure, temperature, and bulk fluid composition.

Finally, it is worth mentioning that although we did not find evidences showing marcasite to pyrite formation in this work, this does not rule out marcasite as a possible reaction intermediate for pyrite formation in Nature. If the marcasite formed in this study were annealed at a higher temperature (>425 °C under vacuum), marcasite would transform to pyrite, according to earlier published works on the solid-state marcasite to pyrite transformation (e.g., Fleet 1970; Lennie and Vaughan 1992; Murowchick 1992). Extrapolations of rates of reaction for the solid-state reaction of marcasite to pyrite based on the kinetic study by Lennie and Vaughan (1992) suggest that it would take around 23 000 yr to yield 50% transformation at 300 °C.

Acknowledgments

This work was funded by Australian Research Council Projects (DP0772299 and DP1095069), the South Australian Museum, and a Ph.D. scholarship to Gujie Qian by the University of South Australia and Ian Wark Research Institute. We acknowledge Adelaide Microscopy Centre staff Leonard Green for assistance in using the EDAX-TSL-EBSD system and EBSD data analysis. We also thank Associate Editor Simon Redfern, and an anonymous reviewer for their valuable comments and suggestions, which greatly improved this paper. Pascal V. Grundler (Adelaide University) is thanked for setting up the vacuum line and the glove box.

References cited

Alsen, N. (1925) Roentgenographische Untersuchungen der Kristallstrukturen von Magnetkies, Breithauptit, entlandit, Millerit und verwandten Verbindungen. Geologiska Foereningens i Stockholm Foerhandlingar, 47, 19–73.

Augustithis, S.S. (1995) Atlas of the textural patterns of ore minerals and metallogenic processes. Walter de Gruyter, Berlin.

Benning, L.G., Wilkin, R.T., and Barnes, H.L. (2000) Reaction pathways in the Fe–S system below 100°C. Chemical Geology, 167, 25–51.

Berner, R.A. (1970) Sedimentary pyrite formation. American Journal of Science, 268, 1–23.

Bethke, C.M. (2008) Geochemical and Biogeochemical Reaction Modeling (2nd ed.). Cambridge University Press, New York, pp. 564.

Brugger, J., McFadden, A., Lenehan, C.E., Etschmann, B., Xia, F., Zhao, J., and Pring, A. (2010) A novel route for the synthesis of mesoporous and low-thermal stability materials by coupled dissolution-reprecipitation reactions: Mimicking hydrothermal mineral formation. CHIMIA, 64, 693–698.

Buerger, M.L. (1931) The crystal structure of marcasite. American Mineralogist, 16, 361–395.

Butler, I.B., Böttcher, M.E., Rickard, D., and Oldroyd, A. (2004) Sulfur isotope partitioning during experimental formation of pyrite via the polysulfide and hydrogen sulfide pathway: implications for the interpretation of sedimentary and hydrothermal pyrite isotope records. Earth and Planetary Science Letters, 228, 495–509.

Drobner, E., Huber, H., Wachtershauser, G., Rose, D., and Stetter, K.O. (1990) Pyrite formation linked with hydrogen evolution under anaerobic conditions. Nature, 346, 742–744.

Einaudi, M.T. (1971) The intermediate product of pyrrhotite alteration. American Mineralogist, 56, 1297–1302.

Fleet, M.E. (1970) Structural aspects of the marcasite-pyrite transformation. Canadian Mineralogist, 10, 225–231.

——— (1978) The pyrrhotite-marcasite transformation. Canadian Mineralogist, 16, 31–35.

Geisler, T., Pidgeon, R.T., Kurtz, R., Bronswijk, W.V., and Schleicher, H. (2003) Experimental hydrothermal alteration of partially metamict zircon. American Mineralogist, 88, 1496–1513.

Harmandas, N.G., Fernandez, E.N., and Koutsoukos, P.G. (1998) Crystal growth of pyrite in aqueous solutions. Inhibition by organophosphorus compounds. Langmuir, 14, 1250–1255.

Hunter, B.A. (1998) Rietica-a visual Rietveld program. International Union of Crystallography Commission on Powder Diffraction Newsletter, 20, 21–23.

Koto, K., Morimoto, N., and Gyobu, A. (1975) The superstructure of the intermediate pyrrhotite. I. Partially disordered distribution of metal vacancy in the 6C type, $Fe_{11}S_{12}$. Acta Crystallographica, B31, 2759–2764.

Lennie, A.R. and Vaughan, D.J. (1992) Kinetics of the marcasite-pyrite transformation: An infrared spectroscopic study. Ametican Mineralogist, 77, 1166–1171.

Mernagh, T.P., Heinrich, C.A., and Mikucki, E.J. (2004) Temperature gradients recorded by fluid inclusions and hydrothermal alteration at the Mount Charlotte gold deposit, Kalgoorlie, Australia. Canadian Mineralogist, 42, 1383–1403.

Murowchick, J.B. (1992) Marcasite inversion and the petrographic determination of pyrite ancestry. Economic Geology, 87, 1141–1152.

Murowchick, J.B. and Barnes, H.L. (1986) Marcasite precipitation from hydrothermal solutions. Geochimica et Cosmochimica Acta, 50, 2615–2629.

Pewkliang, B., Pring, A., and Brugger, J. (2008) The formation of precious opal: clues from the opalization of bone. Canadian Mineralogist, 46, 139–149.

Pokrovskii, V.A. (1999) Calculation of the standard partial molal thermodynamic properties and dissociation constants of aqueous HCl^0 and HBr^0 at temperatures to 1000 °C and pressures to 5 kbar. Geochimica et Cosmochimica Acta, 63, 1107–1115.

Putnis, A. (2002) Mineral replacement reactions: from macroscopic observations to microscopic mechanisms. Mineralogical Magazine, 66, 689–708.

——— (2009) Mineral replacement reactions. In E.H. Oelkers and J. Schott, Eds., Thermodynamics and Kinetics of Water-Rock Interaction, 70, p. 87–124. Reviews in Mineralogy and Geochemistry, Mineralogical Society of America, Chantilly, Virginia.

Putnis, C.V. (2007) An experimental study of the replacement of leucite by analcime. American Mineralogist, 92, 19–26.

Putnis, C.V., Tsukamoto, K., and Nishimura, Y. (2005) Direct observations of pseudomorphism: Compositional and textural evolution at a fluid-solid interface. American Mineralogist, 90, 1909–1912.

Qian, G., Brugger, J., Skinner, W.M., Chen, G.R., and Pring, A. (2010) An experimental study of the mechanism of the replacement of magnetite by pyrite up to 300 °C. Geochimica et Cosmochimica Acta, 74, 5610–5630.

Ramdohr, P. (1980) The Ore Minerals and their Intergrowths, 2nd ed. Pergamon, Oxford.

Rickard, D. and Luther, G.W. III (2007) Chemistry of iron sulfides. Chemical Review, 107, 514–522.

Rickard, D., Grimes, S., Butler, I., Oldroyd, A., and Davies, K.L. (2007) Botanical constraints on pyrite formation. Chemical Geology, 236, 228–246.

Rieder, M., Crelling, J.C., Sustai, O., Drabek, M., Weiss, Z., and Klementova, M. (2007) Arsenic in iron disulfides in a brown coal from the north bohemian basin, Czech Republic. International Journal of Coal Geology, 71, 115–121.

Rietveld, H.M. (1967) Line profiles of neutron powder-diffraction peaks for structure refinement. Acta Crystallographica, 22, 151–152.

——— (1969) A profile refinement method for nuclear and magnetic structures. Journal of Applied Crystallography, 2, 65–71.

Sawada, H. (1996) An electron density residual study of α-ferric oxide. Materials Research Bulletin, 31, 141–146.

Schmitz, P. and Janocha, S. (2000) Films. In Ullmann's Encyclopedia of Industrial Chemistry. Wiley-VCH, Weinheim, DOI: 10.1002/14356007.a11_085.

Schoonen, M.A.A. and Barnes, H.L. (1991) Reactions forming pyrite and marcasite from solution: II. Via FeS precursor below 100 °C. Geochimica et Cosmochimica Acta, 55, 1505–1514.

Suleimenov, O.M. and Seward, T.M. (1997) A spectrophotometric study of hydrogen sulphide ionisation in aqueous solutions to 350 °C. Geochimica et Cosmochimica Acta, 61, 5187–5198.

Sung, Y.-H., Brugger, J., Ciobanu, C.L., Pring, A., Skinner, W., and Nugus, M. (2009) Invisible gold in arsenian pyrite and arsenopyrite from a multistage Archaean gold deposit: Sunrise Dam, Eastern Goldfields Province, Western Australia. Mineralium Deposita, 44, 765–791.

Taylor, P., Rummery, T.E., and Owen, D.G. (1979a) Reactions of iron monosulfide solids with aqueous hydrogen sulfide up to 160 °C. Journal of Inorganic and Nuclear Chemistry, 41, 1683–1687.

——— (1979b) On the conversion of mackinawite to greigite. Journal of Inorganic and Nuclear Chemistry, 41, 595–596.

Tenailleau, C., Pring, A., Etschmann, B., Brugger, J., Grguric, B., and Putnis, A. (2006) Transformation of pentlandite to violarite under mild hydrothermal conditions. American Mineralogist, 91, 706–709.

Testemale, D., Brugger, J., Liu, W.H., Etschmann, B., and Hazemann, J.L. (2009) In-situ X-ray absorption study of Iron(II) speciation in brines up to supercritical conditions. Chemical Geology, 264, 295–310.

Thomas, J.E., Skinner, W.M., and Smart, R. St.C. (2001) A mechanism to explain sudden changes in rates and products for pyrrhotite dissolution in acid solution. Geochimica et Cosmochimica Acta, 65, 1–12.

Tokonami, N., Nishiguchi, K., and Morimoto, N. (1972) Crystal structure of a monoclinic pyrrhotite (Fe_7S_8). American Mineralogist, 57, 1066–1080.

Vaughan, D.J. and Craig, J.R. (1978) Mineral Chemistry of Metal Sulfides. Cambrige University Press, U.K.

Wang, H. and Salveson, I. (2005) A review on the mineral chemistry of the non-stoichiometric iron sulphide, $Fe_{1-x}S$ ($0 \le x \le 0.125$): polymorphs, phase relations and transitions, electronic and magnetic structures. Phase Transitions, 78, 547–567.

Wang, H., Pring, A., Ngothai, Y., and O'Neill, B. (2006) The kinetics of the $\alpha \rightarrow \beta$ transition in synthetic nickel monosulfide. American Mineralogist, 91, 171–181.

Watson, E.B. and Cherniak, D.J. (1997) Oxygen diffusion in Zircon. Earth and Planetary Science Letters, 148, 527–544.

Widler, A.M. and Seward, T.M. (2002) The adsorption of gold(I) hydrosulphide complexes by iron sulphide surfaces. Geochimica et Cosmochimica Acta, 66, 383–402.

Wilkin, R.T. and Barnes, H.L. (1996) Pyrite formation by reactions of iron monosulfides with dissolved inorganic and organic sulfur species. Geochimica et Cosmochimica Acta, 60, 4167–4179.

Wu, R., Zheng, Y.F., Zhang, X.G., Sun, Y.F., Xu, J.B., and Jian, J.K. (2004) Hydrothermal synthesis and crystal structure of pyrite. Journal of Crystal Growth, 266, 523–527.

Wyckoff, R.W.G. (1963) Crystal structures (vol. 1). Wiley, New York.

Xia, F., Zhou, J.W., Brugger, J., Ngothai, Y., O'Neil, B. Chen, G.R., and Pring, A. (2008) Novel route to synthesize complex metal sulfides: Hydrothermal coupled dissolution–reprecipitation replacement reactions. Chemistry of Materials, 20, 2809–2817.

Xia, F., Brugger, J., Chen, G.R., Ngothai, Y., O'Neill, B., Putnis, A., and Pring, A. (2009a) Mechanism and kinetics of pseudomorphic mineral replacement reactions: A case study of the replacement of pentlandite by violarite. Geochimica et Cosmochimica Acta, 73, 1945–1969.

Xia, F., Brugger, J., Ngothai, Y., O'Neill, B., Chen, G.R., and Pring, A. (2009b) Three dimensional ordered arrays of zeolite nanocrystals with uniform size and orientation by a pseudomorphic coupled dissolution-reprecipitation replacement route. Crystal Growth & Design, 9, 4902–4906.

Zhao, J., Brugger, J., Grundler, P.V., Xia, F., Chen, G.R., and Pring, A. (2009) Mechanism and kinetics of a mineral transformation under hydrothermal conditions: Calaverite to metallic gold. American Mineralogist, 94, 1541–1555.

Manuscript received September 14, 2010
Manuscript accepted June 20, 2011
Manuscript handled by Simon Redfern